

Dear Editor and Reviewer #2,

Following final comment by Reviewer #2 (below), we introduced description of the performed filtration for the vertical velocity component, as requested by Reviewer #2.

**Reviewer #2:** The authors are mute on specific details on how to separate good and bad data in this situation. Without solid proof, this approach does not seem to be appropriate. Therefore, I suggest filtering out suspicious data from Fig. 8, showing only those velocities for which the authors are sure of their quality. Some modifications of the Data section (Section 2) describing the performed filtration would also be helpful.

Following this comment, we:

- (i) Omitted text in lines 360-368;
- (ii) Introduced new text in section 3 (Methods) in lines 149-161: ***“Using vertical velocity for DVM interpretation is not intuitive. The vertical velocity component is very sensitive to spatial inhomogeneity of the flow field and errors in the ADCP tilt angle, introducing errors and significant contamination to the measured vertical velocity component (Ott, 2005). Deviations of the vertical velocity diurnal pattern can also be attributed to a more dynamical (turbulent) state of the environment associated with high-velocity currents. In what follows, we are only interested in the vertical velocity estimates, which are sensitive to the MVBS diurnal cycling. For this analysis, the vertical velocity time series were filtered as following. We removed diurnal cycling and low frequency variability using 24-hour and 90-day running mean, respectively. All velocity values exceeding one standard deviation of the mean for the residual time series are considered as noise attributed to spatial inhomogeneity of the flow field and errors in the ADCP tilt angle. In what follows, we show that the contaminated vertical velocity data assigned to upwellings, downwellings, and eddies. Thus, they cannot be used for interpretation of DVM modifications imposed by these major high-velocity events. Therefore, our analysis on impact of the major energetic events on DVM is entirely based on vertical redistribution of the acoustic backscatters”***;
- (iii) We modified Figure 8 depicting time periods when vertical velocity data are considered to be contaminated (at the top of Figure 8c);
- (iv) We added new text in the Figure 8 caption in lines 1017-1020: ***“Horizontal black lines at the top of panel (c) depict periods of noise in vertical velocity attributed to spatial inhomogeneity of the flow field and errors in the ADCP tilt angle (for more details see section 3)”***.

On behalf of the authors,

Igor Dmitrenko

# 1 **Sea-ice and water dynamics and moonlight impact the acoustic** 2 **backscatter diurnal signal over the eastern Beaufort Sea** 3 **continental slope**

4

5 Igor A. Dmitrenko<sup>1</sup>, Vladislav Petrusevich<sup>1</sup>, Gérald Darnis<sup>2</sup>, Sergei A. Kirillov<sup>1</sup>, Alexander S.  
6 Komarov<sup>3</sup>, Jens K. Ehn<sup>1</sup>, Alexandre Forest<sup>2</sup>, Louis Fortier<sup>2</sup>, Søren Rysgaard<sup>1,4</sup> and David G.  
7 Barber<sup>1</sup>

8 <sup>1</sup>Centre for Earth Observation Science, University of Manitoba, Winnipeg, R3T 2N2, Canada

9 <sup>2</sup>Department of Biology, Laval University, Québec City, G1V 0A6, Canada

10 <sup>3</sup>Data Assimilation and Satellite Meteorology Research Section, Environment and Climate Change Canada,  
11 Ottawa, K1G 3Z4, Canada

12 <sup>4</sup>Arctic Research Centre, Aarhus University, Aarhus, DK-8000, Denmark

13 *Correspondence to:* Igor A. Dmitrenko (igor.dmitrenko@umanitoba.ca)

14 **Abstract.** A two-year-long time series of currents and acoustic backscatter from an Acoustic Doppler Current  
15 Profiler, moored over the eastern Beaufort Sea continental slope from October 2003 to September 2005, were  
16 used to assess dynamics and variability of the sound-scattering layer. It has been shown that acoustic backscatter  
17 is dominated by a synchronized diel vertical migration (DVM) of the zooplankton. Our results show that DVM  
18 timings (i) were synchronous with sunlight, and (ii) were modified by moonlight and sea-ice, which attenuates  
19 light transmission to the water column. Moreover, DVM is modified or completely disrupted during highly  
20 energetic current events. Thicker ice observed during winter-spring 2005 lowered the backscatter values, but  
21 favored extending DVM toward the midnight sun. In contrast to many previous studies, DVM occurred through  
22 the intermediate water layer during the ice-free season of the midnight sun in 2004. In 2005, the midnight sun  
23 DVM was likely impacted by a high acoustic scattering generated by suspended particles. During full moon at  
24 low cloud cover, the nighttime moonlight illuminance led to zooplankton avoidance of the sub-surface layer  
25 disrupting DVM. Moreover, DVM was disrupted by upwelling, downwelling and eddy passing. We suggest that  
26 these deviations are consistent with DVM adjusting to avoid enhanced water dynamics. For upwelling and  
27 downwelling, zooplankton likely respond to the along-slope water dynamics dominated by surface- and depth-  
28 intensified flow, respectively. This drives zooplankton to adjust DVM by aggregating in the low or upper  
29 intermediate water layer for upwelling and downwelling, respectively. The baroclinic eddy reversed DVM below  
30 the eddy core.

## 31 **1 Introduction**

32 The acoustic backscatter signal recorded in the ocean by acoustic Doppler current profilers (ADCPs) is mainly  
33 dominated by zooplankton. The diurnal patterns of the acoustic backscatter signal are comprised of diel vertical  
34 migration (DVM) of zooplankton, the synchronized movement of zooplankton up and down in the water column  
35 over a daily cycle (e.g., Brierley, 2014). In terms of biomass, DVM is arguably the largest daily migration of  
36 animals on earth (Hays, 2003), and the largest non-human migration (Brierley et al., 2014). DVM has been  
37 extensively explored in the Arctic using either echo sounders or zooplankton nets (e.g., Kosobokova, 1978;  
38 Fortier, et al., 2001; Blachowiak-Samolyk et al., 2006; Cottier et al., 2006; Falk-Petersen et al., 2008). The latest

39 progress in assessing DVM in the Arctic is related to understanding DVM during the Arctic polar night (Berge et  
40 al., 2009, 2015) and the role of moonlight in modifying DVM (Last et al., 2016; Petrusевич et al., 2016). While  
41 significant progress has been achieved in understanding DVM, the sea-ice and ocean dynamics control on DVM  
42 in the Arctic environment remains poorly appreciated.

43 ADCPs moored over the entire annual cycle in the seasonally ice-covered Arctic water provide a unique  
44 temporal evolution of the DVM patterns. This seasonal perspective is essential to achieve a more complete and  
45 quantitative understanding of DVM in response to the light and sea-ice conditions (e.g., Tran et al., 2016; Hobbs  
46 et al., 2018). Here we assess temporal evolution of the DVM patterns using a two-year-long time series of velocity  
47 and acoustic backscatter from an ADCP-equipped mooring deployed over the upper eastern Beaufort Sea  
48 continental slope from October 2003 to September 2005 (Figure 1). The ADCP limitation, however, comes from  
49 its ability to detect only the biomass moving at a population level, i.e., comprising the migrating sound-scattering  
50 layer (Hobbs et al., 2018).

51 The oceanographic factors controlling DVM in the seasonally ice-covered Arctic areas, located at the  
52 inner border of the polar circle, remains poorly assessed. Here we use observations from the oceanographic  
53 mooring located at  $\sim 71^\circ\text{N}$ , the area, where the Sun is between  $0$  and  $<6^\circ$  below the horizon all day on the winter  
54 solstice. At this latitude no actual daylight is experienced during short winter daylight hours with the exception of  
55 civil twilight when solar illumination is still sufficient for the human eye to distinguish terrestrial objects. This  
56 geographical position makes our DVM observational site vastly different from those at Svalbard (astronomical  
57 twilight, the Sun is between  $12$  and  $18^\circ$  below the horizon,  $\sim 80^\circ\text{N}$ ; e.g., Grenvald et al., 2016; Darnis et al., 2017),  
58 Canada Basin (nautical twilight, the Sun is between  $6$  and  $12^\circ$  below the horizon,  $\sim 77.5^\circ\text{N}$ ; La et al., 2018), and  
59 Northeast Greenland (nautical twilight,  $\sim 74.5^\circ\text{N}$ , Petrusевич et al., 2016). Civil twilight is observed at the CA13  
60 latitude from 19 November to 21 January. For the winter solstices (22 December), the civil twilight lasts for about  
61 3 h. The polar day (or the midnight sun, the Sun is above the horizon for the entire 24 hours) lasts at the CA13  
62 latitude from 10 May to 1 August.

63 This study is built on results by Dmitrenko et al. (2018) on water dynamics over the eastern Beaufort Sea  
64 continental slope taking advantage of using the ADCP-derived acoustic backscatter for temporal appreciation of  
65 DVM patterns during two consecutive annual cycles. Our particular focus is on the DVM modifications, caused  
66 by wind-forced upwelling and downwelling over the Beaufort Sea continental slope, and the different types of  
67 sea-ice cover. We also add more data points and further proof to research focused on the effect of moonlight on  
68 DVM (e.g., Webster et al., 2015; Last et al., 2016; Petrusевич et al., 2016).

## 69 **2 Data**

70 We used data from the ArcticNet oceanographic mooring CA13 deployed over the upper Canadian Beaufort Sea  
71 continental slope at 300-m depth from 9 October 2003 to 4 September 2005 at  $71^\circ 21.356' \text{N}$ ,  $131^\circ 21.824' \text{W}$   
72 (Figure 1). The mooring description can be found in Dmitrenko et al. (2016). For this study, we used (i) velocity  
73 and acoustic backscatter intensity records from a 300 kHz upward-looking Workhorse Sentinel ADCP by  
74 Teledyne RD Instruments (RDI) at 119-m depth and (ii) temperature records from the moored CTD (conductivity-  
75 temperature-depth) SBE-37 by Sea-Bird Electronics, Inc. at 49-m and 119-m depth. The velocity and acoustic  
76 backscatter data were obtained at 8-m depth intervals, with a 1-h ensemble time interval and 30 pings per  
77 ensemble. The first bin was located at  $\sim 9$  m above the transducer, i.e., at 108 m depth. For this research, we used

78 bins at 28, 68, and 108 m depth. Data at 48 and 88 m depth were obtained by linear interpolation between bins at  
79 44 m and 52 m, and 84 m and 92 m, respectively. The RDI ADCP precision and resolution are  $\pm 0.5\%$  and  $\pm 0.1$   
80  $\text{cm s}^{-1}$ , respectively. The standard deviation for an ensemble average of 30 pings for the 8-m depth cell size is  
81 reported by RDI to be  $1.19 \text{ cm s}^{-1}$ . The accuracy of the ADCP vertical velocity measurements is not validated;  
82 however, for the 600 kHz RDI ADCP, Wood and Gartner (2010) reported that the vertical velocity is more  
83 accurate than the horizontal velocity by at least a factor of two. The compass accuracy is  $\pm 2^\circ$ . The magnetic  
84 deviation was added. The along-slope direction was determined to be  $64^\circ\text{T}$  ( $^\circ\text{T}$  - the direction measured with  
85 reference to the true north) using the scatterplot of the daily mean velocity data following an assumption that the  
86 maximum dispersion of velocity measurements occurs along the continental slope (Dmitrenko et al., 2016).  
87 Mooring data were complemented by the vertical CTD, chlorophyll fluorescence and particulate beam attenuation  
88 profiles taken at mooring deployment and recovery in October 2003 and September 2005, respectively, and in  
89 July 2004 using a CTD probe SBE-911 (Figure 2). According to the manufacturers' estimates, individual  
90 temperature and conductivity measurements are accurate to  $\pm 0.001^\circ\text{C}$  and  $\pm 0.0003 \text{ S m}^{-1}$ , respectively, for the  
91 SBE-911, and to  $\pm 0.002^\circ\text{C}$  and  $\pm 0.0003 \text{ S m}^{-1}$  for SBE-37.

92 The total cloud cover (%) for the mooring location is obtained from the National Centers for  
93 Environmental Prediction - NCEP (Kalnay et al., 1996). The accuracy of the cloud cover data is uncertain.  
94 Comparing the satellite- to NCEP-derived cloud cover over the Arctic ( $60^\circ\text{-}90^\circ\text{N}$ ) for 2000-2014 shows that  
95 NCEP data underestimates the mean cloud cover amount by about 25-30% all year round (Liu and Key, 2016).

96 For sea-ice, we use the following five different data sets. (i) Sea-ice concentrations (Figure 3b) are  
97 derived from the Advanced Microwave Scanning Radiometer for EOS (AMSR-E) with errors less than 10% for  
98 ice concentrations above 65% (Spren et al., 2008). They have been computed by applying the ARTIST Sea Ice  
99 (ASI) algorithm to brightness temperatures measured with the 89 GHz AMSR-E channels and are available  
100 through <https://icdc.cen.uni-hamburg.de/en/seaiceconcentration-asi-amsre.html>. The ASI algorithm is described  
101 in Spren et al. (2008). The spatial grid resolution for ice concentration is 6.25 km, and we used data from the  
102 pixel, closest to the mooring position.

103 For sea ice thickness, we used (ii) grid daily data from the Pan-Arctic Ice Ocean Modeling and  
104 Assimilation System (PIOMAS, <http://psc.apl.uw.edu/research/projects/arctic-sea-ice-volume-anomaly/data/>)  
105 developed at the Polar Science Center, University of Washington. PIOMAS is a coupled ocean and sea ice model  
106 that assimilates daily sea-ice concentration and sea surface temperature satellite products (Zhang and Rothrock,  
107 2003). We used data from the grid node at  $71.3^\circ\text{N}$ ,  $133.3^\circ\text{W}$  closest to the mooring position. Schweiger et al.  
108 (2011) reported, that PIOMAS spatial thickness patterns agree well with Ice, Cloud, and land Elevation Satellite  
109 (ICESat) thickness estimates (also used in this study) with pattern correlations of above 0.8. However, PIOMAS  
110 tends to overestimate thicknesses for the thin ice area around the Beaufort Sea, and underestimate the thick ice  
111 area around northern Greenland and the Canadian Arctic Archipelago (Wang et al., 2016). The overall differences  
112 between PIOMAS and ICESat is -15% or -0.31 m (Wang et al., 2016). As an alternative source of sea-ice thickness  
113 data, we used (iii) simulations based on the Hybrid Coordinate Ocean Model (HYCOM, v2.2.98; e.g. Chassignet  
114 et al., 2007) + Community Ice Code (CICE, v4.0; e.g. Hunke, 2001) coupled ocean and sea ice system, developed  
115 at the Danish Meteorological Institute (DMI, Madsen et al., 2016). The horizontal resolution is  $\sim 10 \text{ km}$ . The model  
116 domain covers the Arctic Ocean and the Atlantic Ocean down to  $\sim 20^\circ\text{S}$ . Madsen et al. (2016) reported that the  
117 simulated sea-ice thickness distribution near the Canadian Arctic Archipelago and the northern coast of Greenland

118 is consistent with CryoSat-2 satellite measurements and the NASA Operation IceBridge airborne observations.  
119 Simulated sea-ice thicknesses, shown in Figure 3b, were derived for the grid node closest to the mooring position.  
120 Spatial distributions of sea-ice thickness (Figures 4, 6e, and 6f) were acquired from  
121 <http://ocean.dmi.dk/arctic/icethickness/thk.uk.php>.

122 (iv) We also used data on sea-ice thickness from ICESat obtained from the NASA National Snow and  
123 Ice Data Center – NSIDS (Yi and Zwally, 2009). Data represent the gridded 25-km means. Kwok et al. (2007)  
124 found a mean uncertainty of the sea-ice thickness of about 0.7 m, and the sea-ice draft estimated from ICESat data  
125 relative to that measured at moorings agreed within 0.5 m. We use data from the ICESat campaigns previously  
126 used by Kwok et al. (2009): ON03 (24 September - 18 November 2003), FM04 (17 February – 23 March 2004),  
127 ON04 (3 October – 8 November 2004), and FM05 (17 February – 24 March 2005) shown in Figure 5. Finally, we  
128 used (v) satellite synthetic aperture radar (SAR) imagery acquired by Canadian RADARSAT over the mooring  
129 location before the sea-ice breakup in 2004 and 2005 (Figures 6a-6d). RADARSAT data were acquired through  
130 the Government of Canada’s Earth Observation Data Management System ([https://www.eodms-sgdot.nrcan-](https://www.eodms-sgdot.nrcan-mcan.gc.ca)  
131 [mcan.gc.ca](https://www.eodms-sgdot.nrcan-mcan.gc.ca)).

132 Snow depth over sea-ice, derived from AMSR-E/Aqua, was obtained from NSIDC (Cavalieri et al.,  
133 2014). The 12.5 km snow depth is provided as a 5-day running average. It is generated using the AMSR-E snow-  
134 depth-on-sea-ice algorithm based on the spectral gradient ratio of the 18.7 GHz and 36.5 GHz vertical polarization  
135 channels (Markus and Cavalieri, 1998). As of the AMSR-E sea-ice concentrations, for generating time series of  
136 the snow depth over sea-ice (Figure 3a) we used data from the pixel closest to the mooring position.

### 137 **3 Methods**

138 We analyzed the acoustic backscatter and velocity time series from ADCP to reveal modifications of the acoustic  
139 backscatter diurnal signal primarily dominated by DVM. In general, the particles in the water column producing  
140 a significant portion of acoustic backscatter comprise suspended sediments or planktonic organisms (e.g.,  
141 Petrusevich et al., 2020). Frazil ice crystals also generate an enhanced acoustic backscatter (e.g., Dmitrenko et al.,  
142 2010). However, sound scattering produced by zooplankton is more complex compared to that generated by  
143 sediment particles due to DVM (Stanton et al., 1994). Moreover, ADCPs, unlike echo-sounders, are limited in  
144 deriving accurate quantitative estimates of zooplankton biomass (Lemon et al., 2001, 2012; Vestheim et al., 2014).  
145 This is mainly due to calibration issues (Brierley et al., 1998; Fielding et al., 2004; Lemon et al., 2008; Lorke et  
146 al., 2004) and the beam geometry (Vestheim et al., 2014). To account for the beam geometry, we derived mean  
147 volume backscatter strength (MVBS) in dB from the acoustic backscatter echo intensity following the procedure  
148 described by Deines (1999).

149 Using vertical velocity for DVM interpretation is not intuitive. The vertical velocity component is very  
150 sensitive to spatial inhomogeneity of the flow field and errors in the ADCP tilt angle, introducing errors and  
151 significant contamination to the measured vertical velocity component (Ott, 2005). Deviations of the vertical  
152 velocity diurnal pattern can also be attributed to a more dynamical (turbulent) state of the environment associated  
153 with high-velocity currents. In what follows, we are only interested in the vertical velocity estimates, which are  
154 sensitive to the MVBS diurnal cycling. For this analysis, the vertical velocity time series were filtered as  
155 following. We removed diurnal cycling and low frequency variability using 24-hour and 90-day running mean,  
156 respectively. All velocity values exceeding one standard deviation of the mean for the residual time series are

157 considered as noise attributed to spatial inhomogeneity of the flow field and errors in the ADCP tilt angle. In what  
158 follows, we show that the contaminated vertical velocity data assigned to upwellings, downwellings, and eddies.  
159 Thus, they cannot be used for interpretation of DVM modifications imposed by these major high-velocity events.  
160 Therefore, our analysis on impact of the major energetic events on DVM is entirely based on vertical redistribution  
161 of the acoustic backscatters.

162 Under-ice illumination was modelled using the exponential decay radiative transfer model (Grenfell and  
163 Maykut, 1977; Perovich, 1996). Figure 3c shows the sea-surface illuminance at mooring position computed for  
164 the open water conditions (no sea-ice and snow cover). Transmittance through the sea ice and snow cover to depth  
165  $z$  in the ice was calculated using the following equation:  $T(z) = i_0 e^{-K_t z}$ , where  $i_0$  is the fraction of the wavelength-  
166 integrated incident irradiance transmitted through the top 0.1 m of the surface layer, and  $K_t$  is the total extinction  
167 coefficient in the snow or sea ice cover. The values adopted for the sea ice and snow covers were  $i_0=0.63$ ,  $K_t=1.5$ ,  
168 and  $i_0=50.9$ ,  $K_t=0.1$ , respectively (Grenfell and Maykut, 1977). For computing under-ice illumination in Figures  
169 3d and 3e, we use PIOMAS and HYCOM+CICE data on the simulated sea-ice thickness, respectively. The snow  
170 thickness on the top of the ice was taken from AMSR-E/Aqua observations. We accounted for the sea-ice and  
171 snow cover if the sea-ice concentration exceeds 90%. Cloud cover information was not utilized by this model  
172 taking due to high uncertainty of the cloud cover data (Liu and Key, 2016).

173 Time series of MVBS (Figures 7c-7g), vertical velocity component (Figures 8c-8g) and surface layer  
174 illumination (Figures 7b and 8b), computed for the HYCOM+CICE sea-ice thickness, are presented in a form of  
175 actograms showing a rhythm of activity. Variations during a day-long period are presented along the vertical axis  
176 of the actogram, while the long-term patterns of diurnal behavior can be assessed following the horizontal axis (e.  
177 g., Leise et al., 2013; Last et al., 2016; Hobbs et al., 2018). For the actograms of illuminance we introduced an  
178 artificial visual boundary on the illuminance colour scheme at 1 lux (gray to orange), the threshold, which  
179 corresponds to illuminance during the deep twilight.

180 Following Barber et al. (2015), we used the kinetic energy,  $E = (U^2 + V^2) / 2$ , derived from the zonal ( $U$ )  
181 and meridional ( $V$ ) components of the current velocity to identify the major energetic events exceeding the two  
182 standard deviation threshold of  $\sim 500 \text{ cm}^2 \text{ s}^{-2}$ . Using this threshold, Dmitrenko et al. (2018) identified thirteen  
183 major energetic events comprised of upwellings and downwellings. They are highlighted in Figures 7-9 with blue  
184 and pink shadings, respectively.

## 185 **4 Sea-Ice and Oceanographic Settings**

### 186 **4.1 Sea-ice**

187 The southern Beaufort Sea is seasonally ice-covered. It is dominated by the first-year pack ice with thickness  
188 gradually increasing from zero in September to  $\sim 80$ -90 cm in March-April (Melling et al., 2005). In the Canada  
189 Basin beyond the eastern Beaufort Sea continental slope, ice conditions are partly dominated by the multi-year  
190 pack ice with a mean thickness increasing from about 30 cm in August-September to 210-220 cm in May  
191 (Krishfield et al., 2014). The multi-year Greenland pack ice ( $>7$  m thick) occupies the area to the north of the  
192 Canadian Arctic Archipelago and Greenland (e.g., Kwok et al., 2009).

193 The on-slope displacement of the multi-year pack ice from the Greenland and Ellesmere Island shelves  
194 was observed during winter 2005. This is evident from the sea-ice thickness ICESat data showing a west-  
195 southward expansion of the Greenland pack in February - March 2005 (Figure 5d). This is in line with detecting

196 multi-year ice on the RADARSAT satellite imagery acquired over the mooring position in May 2005 (Figure 6).  
197 The lighter areas in Figures 6c and 6d indicate the multi-year pack ice expanded over the mooring position before  
198 the sea-ice breakup in May 2005.

199 The satellite information on sea-ice thickness, however, is not consistent with PIOMAS. For February-  
200 March 2004 and 2005, PIOMAS provides estimates of sea-ice thickness at mooring position of 1.87 m and 2.28  
201 m, respectively (Figure 3b). In contrast, for the same time period, ICESat provides 1.5-1.4 m and 2.4-2.5 m,  
202 respectively (Figures 4c and 4d). This discrepancy is in line with the conclusions by Wang et al. (2016) that  
203 PIOMAS overestimates thicknesses for the thin ice area around the Beaufort Sea and underestimates the thick ice  
204 area around the northern Greenland and the Canadian Arctic Archipelago. For winter-spring 2003-04, PIOMAS  
205 data agree relatively well with HYCOM+CICE data (Figure 3b). For January-May 2005, however, the discrepancy  
206 between PIOMAS and HYCOM+CICE increases from ~0.5 m on 1 January 2005 to ~1.3 m on 22 May 2005  
207 (Figure 3b). During winter-spring 2005, spatial distribution of sea-ice thickness, derived from HYCOM+CICE  
208 simulations, shows the on-slope displacement of the multi-year pack ice from the Greenland and Ellesmere Island  
209 shelves (Figure 4), which is also revealed from the satellite observations (Figures 5 and 6a-6d). For winter-spring  
210 2005, the HYCOM+CICE data on the multi-year pack ice >2 m thick over the mooring position are in line with  
211 detecting multi-year ice on the RADARSAT satellite imagery acquired before sea-ice breakup in May 2005  
212 (Figure 6). Overall, the HYCOM+CICE simulations and satellite data suggest that during winter-spring 2005 sea-  
213 ice thickness over the mooring location exceeded that for 2004 by ~1 m with important implication for the under-  
214 ice illuminance values as evident from actograms of under-ice illuminance in Figures 3d and 3e. In what follows,  
215 we use under-ice illuminance derived using the HYCOM+CICE simulations.

#### 216 **4.2 Temperature and salinity**

217 The structure of the near-surface and intermediate water layers over the eastern Beaufort Sea upper continental  
218 slope, resolved by ADCP, is comprised of a mixture of river runoff and sea-ice meltwater and seawater of Pacific  
219 origin (Figure 2). A surface layer of relatively warm and low-salinity water (~27-29) is freshened by the  
220 Mackenzie River runoff and sea-ice melt. Water with the salinity  $29 < S < 33$  is generally assigned to Pacific  
221 Water (PW) – e.g., Dmitrenko et al. (2016). It is transported along the Beaufort Sea continental slope by an  
222 Alaskan branch of the PW flow emanating from Bering Strait. The relatively fresh PW layer impacts the halocline  
223 structure, producing a double halocline layer with a low stratified Upper Halocline water formed by the insertion  
224 of PW that overlies Lower Halocline water originating from the Eurasian Basin. In this study, we associated PW  
225 with the broad temperature range between 1.5°C and –1.5°C approximately centered at  $S \sim 32$  residing upper and  
226 low halocline layers (Figure 2). Pacific Summer Water (PSW) is broadly classified here as  $T > -1.2^\circ\text{C}$  and  $30 <$   
227  $S < 32$  (pink shading in Figure 2). In October 2003, July 2004, and September 2005, PSW occupied the upper  
228 intermediate water layer from ~25 to ~60 m depth (Figure 2). This water mass is usually comprised of the Chukchi  
229 Summer water transported through Herald Canyon on the western Chukchi shelf (Woodgate et al., 2005) and the  
230 Alaskan Coastal water transported by the Alaskan coastal current through Barrow Canyon (Pickart et al., 2005).  
231 The underlying Pacific Winter Water (PWW) with the broad temperature minimum below –1.2°C centred at  $S \sim$   
232  $33$  (blue shading in Figure 2) is generated during freezing and brine rejection in the Bering and Chukchi Seas  
233 (Weingartner et al., 1998; Pickart, 2004). During 2003-2005, PWW occupied the lower intermediate water layer  
234 in ~60-140 m depth (Figure 2). The warm and saltier Atlantic water with temperatures above 0°C and  $S > 33.5$

235 underlies PWW at depths > 230 m that significantly exceeds the depth range resolved with ADCP measurements  
236 (Figure 2).

### 237 **4.3 Water dynamics**

238 The kinetic energy of currents over the eastern Beaufort Sea continental slope is mainly affected by the along-  
239 slope current component (Kulikov et al., 1998; Williams et al., 2006; Dmitrenko et al., 2016, 2018). For CA13,  
240 the maximum variability of currents is also consistent with along-slope direction, explaining ~ 70% of the total  
241 velocity variability (Dmitrenko et al., 2018). Thus, major energetic events highlighted in Figures 7-9 are primarily  
242 associated with along-slope flow dynamics, as also follows from the velocity time series in Figures 9c and 9d.  
243 Among thirteen major energetic events in Figures 7-9, four events were clearly attributed to the depth-intensified  
244 flow (#3D, 4D, 6D and 10D; pink shading in Figures 7-9) generated by ocean downwelling superimposed on the  
245 background bottom-intensified eastward shelfbreak flow. Six events are associated with the surface-intensified or  
246 barotropic flow (#1U, 2U, 7U, 8U, 9U, and 12U; blue shading in Figures 7-9). These events were attributed to  
247 ocean upwelling (Dmitrenko et al., 2018). While events #5U and 11U are depth-intensified, they are highlighted  
248 with blue shading because they are consistent with upwelling-favorable atmospheric forcing that usually drives  
249 the surface-intensified events. Vice versa, event #13D is surface-intensified, but it has been highlighted with pink  
250 shading because it is consistent with downwelling-favorable atmospheric forcing (Dmitrenko et al., 2018).

## 251 **5 Diurnal Signal of the Mean Volume Backscatter Strength (MVBS) and Vertical Velocity**

252 MVBS and vertical velocity actograms were computed for the depth of 28, 48, 68, 88 and 108 m (Figures 7c-7g  
253 and 8c-8g). These actograms reveal a rhythm of activity with diurnal cycle seen in the vertical axis of an actogram.  
254 The 2-year long variability of the diurnal cycle is observed along the horizontal axis.

### 255 **5.1 Seasonal patterns**

256 In general, MVBS actograms resemble seasonal variability of the diurnal signal following light conditions  
257 (Figures 7b-7g and 8b-8g). In the subsurface layer (28 m depth), a low MVBS corresponds to a relatively high  
258 illuminance during the day, while an elevated MVBS is consistent with a low illuminance during the night (Figures  
259 7b and 7c). In contrast, at 108 m depth, MVBS shows an opposite pattern with a high MVBS during the light time  
260 of the day and a low MVBS in the darkness (Figures 7b and 7g). This variability in MVBS is consistent with  
261 DVM.

262 In general, the MVBS diurnal signal follows the seasonal variability of the sun illuminance during the  
263 entire year except for the period of the polar day when the diurnal pattern becomes significantly disrupted in the  
264 sub-surface water layer. Outside of the polar day, the diurnal changes in the sun illuminance are opposite to MVBS  
265 for the sub-surface layer, while at 108 m depth this relationship becomes positive. During the polar day, in the  
266 subsurface layer the MVBS diurnal rhythm vanishes (Figure 7c). In spring 2004, the vanishing of the MVBS  
267 diurnal pattern from the beginning of May corresponds to an increase of the midnight under-ice illuminance to  
268 >0.1 lux (Figures 7b and 7c). This modification lagged behind the sea-ice retreat off the mooring location by about  
269 one month (Figures 7a and 7c). In contrast, during spring 2005, significant deviation of the MVBS diurnal rhythm  
270 was delayed by about 3 weeks compared to 2004. The deviation of the MVBS diurnal pattern was recorded once  
271 the sea-ice disappeared from the mooring location on 20 May 2005. Note that the satellite-derived data and



272 HYCOM+CICE simulations for winter-spring 2005 show the sea-ice thickness over the mooring location  
273 exceeding that for 2004 by ~1 m (Figures 4-6). In spring 2005, the midnight under-ice illuminance >1 lux was  
274 lagging that in 2004 by about one week (Figure 7b).

275 For the PW layer, the behavior of the MVBS diurnal signal during the polar day is different from the  
276 sub-surface water layer. From about 1 April to 10 July 2004, the diurnal amplitude of MVBS signal was enhanced  
277 at the 68-108 m depth layer due to MVBS values lowered from ~ -61 to -66 dB during the astronomic midnight  
278  $\pm 3$  h (Figures 7e-7g). In contrast to the preceding and subsequent periods, no seasonal modulation of the MVBS  
279 diurnal cycle was observed at this time. This is in line with illuminance, showing almost no seasonal modulation  
280 during the midnight sun (Figure 7b). For the polar day period in 2005, however, enhancement of the MVBS  
281 diurnal signal seemed to be impacted by the short-term high MVBS events likely generated by intrusions of turbid  
282 water. These events were found to be most pronounced through the PSW layer where intrusions of turbid and  
283 relatively warmer water were observed during mooring recovery (Figures 2c, 7d, and 7e).

284 Following the midnight sun, the MVBS diurnal signal returned once the mooring position becomes 100%  
285 ice-covered since 7 November 2003 and 25 October 2004 (Figures 7a and 7c-7g). This is evident from enhancing  
286 the MVBS difference between the light (> 1 lux) and dark (< 1 lux) time for 28-48 m depth (Figure 7c-7d). The  
287 noticeable feature of the MVBS diurnal signal during civil twilight and the subsequent period until the end of  
288 April is a significant MVBS difference between 2003-2004 and 2004-2005 observed during the dark time through  
289 the entire water column resolved with ADCP observations (Figures 7c-7f). Another noticeable feature of MVBS  
290 during this period is numerous disruptions of the diurnal signal discussed below in sections 5.3.1 and 5.3.2.

291 Behind seasonality of diurnal signal in the MVBS time series, the seasonal cycling of the MVBS vertical  
292 distribution has been revealed (Figures 9a and 9b). For midnight, during low-light conditions from October to  
293 February (civil twilight length exceeds daylight length), MVBS tends to increase with depths from 28 to 108 m  
294 depth (Figure 8a). In March-June, the midnight MVBS shows an opposite tendency (Figure 9a). The MVBS  
295 midnight long-term mean, however, shows almost no difference from 28 to 108 m depth with a long-term mean  
296 of -0.6 dB. The seasonal cycle of the MVBS vertical distribution for the astronomic noon is different. From about  
297 winter to summer solstices, MVBS at 128 m depth exceeds that for 28 m depth by about 8 dB (Figure 9b). In  
298 contrast, during the ice-free period in June-August, the MVBS difference from 28 to 108 m depth tends to decrease  
299 down to about zero in late summer. The long-term mean for the astronomic noon (-5.3 dB, Figure 9b) shows a  
300 general tendency of MVBS to increase with depth.

301 The vertical velocity actograms also show a diurnal pattern around astronomic midnight (Figures 8c-8g)  
302 that is consistent with the MVBS diurnal rhythm in Figures 7d-7h. Net upward movement is regularly observed  
303 before the astronomic midnight once the under-ice dark-time illuminance was <0.1 lux (Figures 8b-8g). Moreover,  
304 the most intense upward flow was recorded during 1-3 h after the illuminance dropped below the 0.1 lux threshold.  
305 In contrast, a downward net flow was recorded following the tendency of under-ice illuminance to increase from  
306 midnight to noon once illuminance exceeds the 0.1 lux threshold (Figures 8b-8g). At the end of April 2004, once  
307 under-ice illuminance exceeded the 0.1 lux threshold for 24 h a day approaching the midnight sun, the vertical  
308 velocity diurnal signal completely vanished. During May-June 2004, however, a weaker net upward and  
309 downward diurnal movement of about  $\pm 0.5$  cm s<sup>-1</sup> was recorded at 68 and 88 m depth from noon to midnight  
310 (light blue to green shading in Figures 8e and 8f), and from midnight to noon (light green to yellow shading in  
311 Figures 8e and 8f), respectively. This is consistent with the MVBS diurnal rhythm revealed through the PW layer

312 during summer 2004 (Figures 7e-7g). Following the under-ice illuminance, well-pronounced velocity diurnal  
313 signal again appeared since end of August 2004 when the midnight under-ice illuminance decreases to the 0.1 lux  
314 threshold gradually returning to civil twilight. In spring 2005, the vertical velocity diurnal signal was relatively  
315 well pronounced until the midnight under-ice illuminance is below the 0.1 lux threshold (Figures 8b-8g). As of  
316 MVBS, complete cessation of a diurnal signal in vertical velocity in spring 2005 was observed at 68-88 m depth  
317 only when sea-ice started to retreat in mid-May (Figure 8a). In this case, complete cessation of diurnal signal  
318 lagged the 0.1 lux threshold by about 20 days (Figures 8b, 8e, and 8f). During the midnight sun 2005, the velocity  
319 diurnal rhythm is unrecognizable.

320 Finally, the velocity diurnal signal varies with depth. The upward and downward flow attributed to diurnal cycling  
321 is higher and less noisy at 68-88 m depth compared to the overlaying sub-surface layer at 28-48 m depth and to a  
322 lesser extent to the underlying water at 108 m depth (Figures 8c-8g).

## 323 **5.2 Moon cycle**

324 During the period of civil twilight when the sun is more than  $6^\circ$  below the horizon, the moonlight was the main  
325 source of illumination over the eastern Beaufort Sea continental slope (Figure 7b). The full moon succeeds with  
326 a mean period of 29.53059 days called a synodic or lunar month. During mid-winter (end of December), the full  
327 moon generates under-ice illuminance up to about 0.001 lux below the sea-ice layer with a thickness of around 1  
328 m and ~20 cm snow depth over sea-ice (Figures 3b and 7b). In contrast, for the open water conditions, the full  
329 moon generates illuminance exceeding 0.1 lux (Figure 3c). Sea-ice strongly attenuates moonlight. Once sea-ice  
330 thickness exceeded ~2.5 m in April 2004 and February 2005, the moonlight transmittance through sea-ice is  
331 completely terminated (Figures 3b and 3e). While the cloud cover attenuates moon illumination, it was not  
332 considered for modelling under-ice illuminance due to high uncertainty of the cloud cover data (Liu and Key,  
333 2016).

334 The MVBS diurnal signal is impacted by the moonlight, also attenuated by the cloud cover. Once the  
335 full moon ( $\pm 6$  days) occurred during the period of civil twilight, the cloud cover shows three low-cloud events  
336 with cloud cover  $\leq 30\%$  (#3, 4 in 2003-2004 and #3 in 2004-2005 in Figures 7a and 7b). During these events, the  
337 MVBS diurnal signal was significantly disrupted in the sub-surface layer, and a low MVBS was observed during  
338 the entire 24 h (Figures 7b and 7c). For the full moon event #4 in January 2004, during the astronomic midnight,  
339 a low MVBS at 28 m depth was associated with an elevated MVBS at 108 m depth, as evident from decreasing  
340 the MVBS difference from 28 to 108 m depth in Figure 9a. Overall, among 14 full moon events occurred in  
341 October-March 2003-2004 and 2004-2005 once the midnight under-ice illuminance was  $< 1$  lux, 3 events in  
342 February-March (#7 in 2004 and #6 and 7 in 2005) show complete cessation of the moonlight transmittance  
343 through sea-ice exceeding 2.5 m thick (Figure 7b). Events #1-5 in 2003-2004 and #1, 2, and 5 in 2004-2005  
344 demonstrated similar anomalies of the MVBS difference from 28 to 108 m depth (Figure 9a). During the noon,  
345 however, this pattern is not obvious (Figure 9b).

346 Full moon event #1 in September-October 2004 gives an example of the moonlight impact on the MVBS  
347 diurnal signal (Figure 7). While the cloud cover during this event was relatively high (~50%, Figure 7a), the dark-  
348 time MVBS dropped by ~2 dB at 28 m depth, but elevated by ~4 dB at 68 and 88 m depth suggesting the downward  
349 displacement of the acoustic backscatters (Figures 7c and 7f-7g, respectively). At noon, however, MVBS elevated  
350 by ~4 dB at 28 m depth (Figure 7c). Note that during this time the under-ice illuminance reduced as the mooring

351 became ice-covered (Figure 7a). It is also important to point out that this full moon event partly overlays with  
352 upwelling #7U described below.

### 353 **5.3 Short-term oceanographic events**

354 The regular diurnal pattern of MVBS was disrupted during the short-term events lasting from several days to  
355 several weeks (Figures 7d-7h). These events also interplay with disruptions generated by moon cycling. We use  
356 actograms of vertical velocity to differentiate disruptions imposed by moonlight from those of dynamic origin  
357 (Figures 8c-8g). In general, the diurnal pattern remains well recognizable during the full moon events (Figures  
358 8b-8g). In contrast, almost all significant or even complete short-term disruptions of the vertical velocity diurnal  
359 rhythm are related to upwelling or downwelling (Figures 8c-8g).

360 ~~The vertical velocity component is very sensitive to spatial inhomogeneity of the flow field and errors in~~  
361 ~~the ADCP tilt angle, introducing errors and significant contamination to the measured vertical velocity component~~  
362 ~~(Ott, 2005). This is consistent with contamination of the vertical velocity data observed during upwellings,~~  
363 ~~downwellings and eddy passing (Figures 8c-8g). Deviations of the vertical velocity diurnal pattern can also be~~  
364 ~~attributed to a more dynamical (turbulent) state of the environment associated with high velocity currents. In what~~  
365 ~~follows, we are only interested in the vertical velocity estimates, which are sensitive to the MVBS diurnal cycling.~~  
366 ~~The contaminated vertical velocity data cannot be used for interpretation of DVM modifications imposed by~~  
367 ~~upwellings, downwellings, and eddies. Therefore, our analysis on impact of the major energetic events on DVM~~  
368 ~~is entirely based on vertical redistribution of the acoustic backscatters (Figures 7c-7g, 9a and 9b).~~

369 Dmitrenko et al. (2018) identified upwelling or downwelling events at CA13 using ADCP velocity data,  
370 the NCEP-derived wind and sea-level atmospheric data, sea surface height records at Tuktoyaktuk (Figure 1) and  
371 numerical simulations. All these events are highlighted in Figures 7-9 with blue and red shadings for upwelling  
372 and downwelling, respectively.

#### 373 **5.3.1 Upwelling Events**

374 Upwelling events disrupt the MVBS diurnal signal in a similar way as the moonlight does. For upwelling #1U,  
375 MVBS at 108 m depth was elevated throughout the full 24 h period (Figure 7g). During the dark time (illuminance  
376  $< 1$  lux) at 28 m depth, MVBS reduced to the end of the event when the surface-intensified flow at 28 m depth  
377 shows maximum velocities exceeding  $30 \text{ cm s}^{-1}$  (Figure 9c). Moreover, upwelling #1U resulted in  $\sim 0.7^\circ\text{C}$   
378 temperature increase at 119 m depth (Figure 9f). Upwelling #2U, occurred right before the winter solstice, shows  
379 significant MVBS reduction at 28-48 m depth gradually vanishing to 108 m depth. Upwelling #5U occurred at  
380 the end of the ice-free season and shortly after the end of the midnight sun 2004. Therefore, the MVBS diurnal  
381 signal was relatively weak and noisy, especially at 28 m depth. However, MVBS increase at 88-108 m depth is  
382 likely attributed to upwelling. Upwelling #7U interplayed with full moon event #1 in September-October 2004. It  
383 seems that the first portion of this event until 3 October 2004 was dominated by the moonlight. Afterward, once  
384 the horizontal velocity at 28 m depth exceeded  $\sim 30 \text{ cm s}^{-1}$  (Figure 9c), a slight reduction of MVBS is observed in  
385 28-48 m depth during the dark time. In contrast to the preceding upwelling events, no elevated MVBS values were  
386 recorded in the overlying water layer. Upwelling #8U completely coincided with full moon event #2 in October-  
387 November 2004. As with the majority of the full moon and upwelling events, it shows the downward redistribution  
388 of the acoustic backscatters from 28-48 m to the deeper water layer (Figures 7c-7g, 9a, and 9b). A similar overlap

389 between full moon and upwelling was observed during upwelling #9U. Significant MVBS reduction within 28-  
390 48 m was accompanied by elevated MVBS in 88-108 m depth during the latter part of this upwelling from 25  
391 November to 5 December 2004. Overall, upwelling events #7-9 resulted in a gradual increase of temperature at  
392 119 m depth from  $-1.55^{\circ}\text{C}$  to  $-0.65^{\circ}\text{C}$  (Figure 9f). Upwelling #11U shows an elevated MVBS during the light  
393 time at 88-108 m (Figures 7f, 7g, and 9b). However, no significant modifications of the MVBS diurnal signal  
394 were observed in the overlying water. The last upwelling #12U in May-June 2005 occurred during the midnight  
395 sun when the MVBS diurnal signal mostly vanished, and MVBS is noisy. We speculate that this noise is due to  
396 the enhanced concentration of suspended particles in the water column (Figure 2c).

397 Overall, among 8 upwelling events observed in 2003-2005, 6 events (#1, 2, 5, 7, 8, 9U) clearly show the  
398 MVBS reduction in the subsurface water layer at 28 m depth (Figure 7c). For upwellings #1, 5, 7, and 8U the  
399 midnight MVBS difference from 28 to 108 m depth tends to decrease, which is consistent with a downward  
400 redistribution of acoustic scatters (Figure 9a). This effect is similar to the MVBS response to the full moon events  
401 as described in section 5.2. It seems that the overlay between the upwelling and full moon can dominate the MVBS  
402 response to upwellings #7-9U (Figures 7b-7g). During the polar day, the MVBS diurnal signal is weak or  
403 completely disrupted, and its response to upwelling is barely traceable (upwelling #12, Figure 7b-7g). Finally,  
404 wind, forcing upwelling events, also impacts the sea-ice cover through the off-shelf displacement of the pack ice  
405 as evident for upwelling event #12 in May-June 2005 (Figure 7a).

### 406 **5.3.2 Downwelling Events**

407 Downwelling events disrupt the MVBS diurnal signal in the opposite way compared to upwellings and moonlight,  
408 moving acoustic backscatters upwards. Downwelling also interferes with MVBS modifications imposed by sea-  
409 ice and the MVBS diurnal signal deviations generated by moonlight. Wind, forcing downwelling events, also  
410 impacts the sea-ice cover through the on-shelf displacement of the pack ice as evident for downwelling events #4,  
411 6 and 13D (Figure 7a). Deviations of the MVBS diurnal signal due to moon cycling interferes with those caused  
412 by downwelling event #3 complicating our analysis.

413 Downwelling #3D occurred at the end of 2003-2004 during civil twilight and strongly interfered with  
414 full moon event #4 (Figure 7). It seems that event #3D is entirely dominated by the moon, disrupting the MVBS  
415 diurnal signal as described in section 5.2. Downwelling #4D was recorded at the end of the polar day 2004 when  
416 the MVBS diurnal signal is terminated at 28-88 m depth (Figures 7c-7f). Wind, forcing downwelling #4D,  
417 displaced pack ice on-shelf, and the CA13 position was reoccupied by sea-ice for about 10 days with implication  
418 for under-ice illuminance. Figures 7c and 7d show that sea-ice and downwelling did not impact MVBS at 28-48  
419 m depth. In contrast, the midnight sun diurnal signal at 68-88 m depth was disrupted due to elevating MVBS at  
420 68-88 m depth during the dark-time (from 22 to 4 h, Figures 7e and 7f). At the same time, the midnight sun diurnal  
421 signal at 108 m depth remained undisturbed (Figure 7g). Downwelling #6D provides the most comprehensive  
422 example of how the MVBS diurnal signal is disrupted by downwelling. In contrast to the full moon and upwelling  
423 events, MVBS at 28-48 m depth was enhanced 24 h a day (Figures 7c and 7d) suggesting the upward redistribution  
424 of the acoustic backscatters from the underlying water layer (Figures 9a and 9b). Note that during this event water  
425 dynamics was dominated by along-slope depth-intensified flow increasing from  $\sim 5\text{ cm s}^{-1}$  at 28 m depth (Figure  
426 9c) to  $>30\text{ cm s}^{-1}$  at 108 m depth (Figure 9d). Downwelling #10D was recorded at the end of civil twilight 2004-  
427 2005. It appears that the beginning of this event is impacted by the full moon (#4, 2004-2005) with the reduction

428 of MVBS in the sub-surface layer at 28 m depth. However, by the end of downwelling #10D, once the bottom-  
429 intensified flow exceeded  $100 \text{ cm s}^{-1}$  at 128 m (Figure 9d), MVBS at 28-48 m depth tended to increase suggesting  
430 the upward redistribution of the acoustic backscatters, similar to downwelling #6D. Downwelling #13D occurred  
431 in mid-August 2005 following the midnight sun. During this time, the MVBS diurnal signal at 28 depth was not  
432 traceable. At 48-88 m depth, the midnight sun diurnal signal was likely masked due to the enhanced concentration  
433 of suspended particles in the water column (Figure 2c).

434 Overall, among 5 downwelling events recorded in 2003-2005, event #6D and partly #10D show  
435 disruption of the MVBS diurnal signal in the sub-surface water layer with MVBS elevated at 28-48 m depth in  
436 response to downwelling. Downwelling events #4 and 13D occurred during and shortly after the midnight sun,  
437 respectively, when the sub-surface MVBS diurnal signal vanishes. Downwelling event #3D was dominated by  
438 the moonlight.

### 439 5.3.3 Eddies

440 Eddies are ubiquitous over the Arctic Ocean continental slope (e.g., Dmitrenko et al., 2008; Pnyushkov et al.,  
441 2018), and particularly over the Beaufort Sea continental slope (e.g., Spall et al., 2008; O'Brien et al., 2011). The  
442 eddy carrying entrained suspended particles was identified by Dmitrenko et al. (2018) based on the ADCP velocity  
443 and acoustic backscatter time series in February–March 2004 (Figures 7 and 10). One more eddy passed mooring  
444 position in December/January 2003/2004 right before downwelling #3D. In Figures 6-8 both eddies are  
445 highlighted with yellow shading.

446 The eddy in February–March 2004 provides an example of how the velocity field attributed to eddy  
447 passing disrupts the MVBS diurnal signal (Figure 10). The greatest tangential speed, exceeding  $22 \text{ cm s}^{-1}$ , marks  
448 the eddy core near 95 m depth (Figures 10a and 10b). Below the core at 119 m depth, a positive temperature  
449 anomaly of  $0.25^\circ\text{C}$  attributed to the eddy passing was recorded on 26 February 2004 (Figure 9f). The velocity  
450 signature of the eddy is hardly discernible shallower than about 50 m, where the temperature anomaly does not  
451 exceed  $\sim 0.1^\circ\text{C}$  (Figures 9e, 10a, and 10b). During the dark time at 108 m depth (below the depth of the greatest  
452 tangential speed), an enhanced MVBS was observed between two maximal of the eddy tangential speed from 27  
453 February to 2 March 2004 (Figure 10d). In contrast, during the daylight, a negative MVBS anomaly was recorded  
454 (Figures 7g and 10d). This completely inverted the MVBS diurnal signal observed at 108 m depth during the eddy  
455 passing. At 28-48 m depth, however, MVBS was not significantly modified. Nevertheless, MVBS was slightly  
456 elevated during the light time (Figures 7c, 7g and 10c). In contrast to water layers above and below the eddy core,  
457 from 26 February to 1 March the MVBS diurnal signal at 68-88 m depth was disrupted by the backscatter  
458 maximum recorded for 24 h a day (Figures 7e and 7f). It appears that this MVBS anomaly is attributed to the  
459 eddy-entrained suspended particles commonly recorded in this area (O'Brien et al., 2011).

460 The eddy in December/January 2003/2004 generated much less MVBS disturbance compared to the one  
461 in February–March 2004 (Figures 7c-7g). The core of the eddy was likely deeper than the ADCP transducer. A  
462 positive temperature anomaly at 119 m depth was  $0.5^\circ\text{C}$  (Figure 9f). A positive MVBS anomaly was recorded  
463 only at 108 m depth during 24 h a day (Figure 7g) likely indicating the eddy-entrained suspended particles. MVBS  
464 in the overlying water layer was not significantly modified.

465 In summary, the eddy in February–March 2004 inverted the MVBS diurnal signal in the water layer  
466 below the eddy core defined by the greatest tangential speed of the horizontal flow. The eddy in December/January  
467 2003/2004 generated no significant MVBS modifications as the eddy core was likely located below the ADCP.

## 468 **6 Discussion**

469 The two-year-long ADCP time series of MVBS and vertical velocity over the upper eastern Beaufort Sea  
470 continental slope are consistent with DVM of zooplankton. MVBS diurnal signal is generated by a diurnal  
471 movement of zooplankton toward the surface at dusk, and descent back the next morning before dawn. DVM  
472 demonstrates predator-avoidance behavior (Hays, 2003). Zooplankton keeps away from a relatively well-  
473 illuminated surface water layer during the light time reducing the light-dependent mortality risk. The acoustic data  
474 from the single-frequency ADCP do not provide any information on the identity of organisms responsible for the  
475 observed DVM patterns, and proper studies on DVM have not been carried out in the Beaufort Sea prior to the  
476 present work. Thus, our analysis is significantly limited by deficiency of zooplankton observations. Moreover, a  
477 comprehensive analysis of the scattering species comprising DVM is logistically impossible for the long-term  
478 deployments in the seasonally ice-covered and remote areas in the high Arctic. This prohibits identification of  
479 specific species whose DVM was detected by the 300 kHz ADCP and altered by the different environmental  
480 factors including illuminance and water dynamics. The deficiency of our analysis clearly defines a necessity for  
481 expanding mooring observations using underwater electronic holographic cameras such as those described by Sun  
482 et al. (2007).

483 In general, DVM at CA13 is controlled by light conditions (Figures 7 and 8). As for the other areas of  
484 the ocean, DVM is triggered by local solar variations, and the timing of migration is sensitive to changes in  
485 seasonal day length (e.g., van Haren and Compton, 2013). Our results show that DVM responds to (i) seasonality  
486 of the sunlight, (ii) seasonality of sea-ice cover that attenuates light transmission to the water column, and to a  
487 lesser extent to (iii) moonlight. Moreover, (iv) DVM can be modified or completely disrupted during highly  
488 energetic current events generated by upwelling, downwelling or eddy passing. Our results also suggest that the  
489 interplay between all these factors impacts DVM at CA13. Furthermore, MVBS is not entirely controlled by  
490 DVM. The suspended particles in the water column enhance acoustic scattering, impacting DVM during the  
491 midnight sun (Figures 2a, and 7b, 7d, and 7e), and also attenuating light intensity in the water column. Below we  
492 discuss all these factors and their impact on DVM in more detail.

### 493 **6.1 DVM seasonal cycle, sea-ice cover, and suspended particles**

494 It appears that DVM is triggered once the estimated near-surface illuminance falls below the 0.1-lux  
495 threshold (Figures 7 and 8). This suggests that the diurnal movement of zooplankton toward the surface at dusk  
496 starts once the near-surface illuminance decreased to  $\sim 0.1$  lux, and descends back the next morning before dawn  
497 as soon as the near-surface illuminance exceeds 0.1 lux. DVM follows changes in seasonal day length, and it stops  
498 at the sub-surface layer as soon as near-surface illuminance retains above  $\sim 0.1$  lux for 24 h a day (Figures 7b-7g).  
499 At the CA13 latitude ( $71^{\circ}21.356'N$ ), the estimated value of near-surface or under-ice illuminance exceeds the 0.1  
500 lux threshold for about 55 and 50 days before the midnight sun in 2004 and 2005, respectively (Figure 7b). During  
501 fall 2004, the sub-surface DVM returned about 27 days after the polar day season, once the midnight near-surface  
502 illuminance dropped below  $\sim 0.1$  lux threshold around 28 August (Figures 6b-6g). Our results on the light threshold

503 are consistent with the preferendum (isolume) hypothesis (e.g., Cohen and Forward, 2009). A variant of the  
504 preferendum hypothesis, the absolute intensity threshold hypothesis, suggests that an ascent at sunset is initiated  
505 once the light intensity decreases below a particular threshold level and a descent at sunrise occurs when the light  
506 intensity increases above the threshold intensity (e.g., Cohen and Forward, 2019). This is in line with our findings  
507 on an absolute 0.1-lux threshold of light, which corresponds to the moonlight illuminance at the gibbous moon  
508 during clear sky (Gaston et al., 2014).

509 The inter-annual variability in estimated under-ice illuminance is entirely attributed to the sea-ice  
510 thickness. During the ice season, the mean cloud cover (~40%) showed insignificant interannual variability  
511 (Figure 7a); thus, the cloud cover was not taken into account. Our results reveal that sea-ice cover modifies the  
512 DVM seasonal cycle by attenuating under-ice illuminance. During winter-spring 2004, CA13 was primarily  
513 covered with the first-year pack ice of about 1.6 m thick (Figures 3b, 4 top, 5a, and 5b). In contrast, during the  
514 same time in 2005, the eastern Beaufort Sea continental slope was occupied by the multi-year pack ice of about  
515 2.6 m thick (Figures 3b, 4 bottom, 5c, and 5d). We suggest that this increased sea-ice thickness extended the DVM  
516 seasonal cycle toward the polar day of 2005. In May 2005, the 0.1-lux threshold estimated for ~2.5 m thick ice  
517 lags that for 2004 by about 5 days (Figure 7b). Following ice-diminished illuminance in April-May 2005, DVM  
518 at 28 m depth was recorded until the beginning of May 2005. Moreover, DVM maintained integrity at 68-108 m  
519 depth until the open-water season started in mid-May 2005 (Figures 7c and 7e-7g, respectively). In contrast, during  
520 spring 2004, DVM vanished about 12 and 28 days ahead of the polar day and open-water season, respectively  
521 (Figures 7). We suggest that this inter-annual DVM variability is consistent with under-ice illuminance. Its  
522 estimated value for mid-May 2004 ( $\geq 10$  lux) exceeds that for May 2005 by a factor of 10 (Figure 7b).

523 The MVBS actograms show asymmetry of the DVM seasonal cycle to the summer solstice (Figures 7b-  
524 7g). In summer 2004, the DVM seasonal cycle terminated about 54 days before the summer solstice but resumed,  
525 lagging summer solstice by 67 days. This asymmetry, being consistent with the estimated 0.1-lux threshold, is  
526 likely attributed to the seasonal sea-ice cover. During spring, the polar day begins when the eastern Beaufort Sea  
527 continental slope is still ice-covered (Figures 6a and 6b), which governs attenuation of light below the ice. In  
528 contrast, after the polar day is ended, the eastern Beaufort Sea continental slope remains ice-free or partly ice-  
529 covered until the end of October allowing sunlight to illuminate the near-surface water layer.

530 In the subsequent winters, the DVM backscatter intensity shows significant interannual variability. The  
531 dark-time MVBS during winter 2003-2004 exceeds that for winter 2004-2005 by ~ 3-5 dB (Figures 7c-7g). We  
532 attribute this inter-annual variability to attenuation of light by a thicker ice cover in winter 2004-2005, as follows  
533 from our preceding discussion. Satellite data and model simulations show that the eastern Beaufort Sea continental  
534 slope was occupied by Greenland pack ice during winter-spring 2005 (Figures 4-6) that results in the reduced  
535 estimate of under-ice illuminance by a factor of 10 (Figure 7b). For example, during full moon events #6 and 7 in  
536 February-March 2005, the night-time moonlight illuminance fell down to the background night-time illuminance  
537  $< 0.0001$  lux (Figure 7b).

538 In general, our results on the sea-ice impact on DVM show that DVM is well synchronized with the  
539 light/dark cycle modified by the sea-ice cover shading. It appears that thicker ice observed during winter 2004-  
540 2005 reduced the backscatter values (Figures 7c-7g), which likely demonstrates a light-mediated response of the  
541 zooplankton involved in DVM. This is in line with Berge et al. (2009) reporting a stronger polar night DVM in  
542 the ice-free Svalbard fjord compared to the ice-covered fjord. Vestheim et al. (2014) reported on shallowing DVM

543 in Oslofjord in response to the freeze-up and subsequent snowfalls. They attributed this shallowing to a relative  
544 reduction of light intensities, which is similar to that observed over the eastern Beaufort Sea continental slope  
545 during winter-spring 2005. La et al. (2015) suggested that sea-ice diminishes DVM signals by blocking the  
546 detectable light intensity for DVM with depth during the Antarctic winter. At the same time, our results contrast  
547 with the observations of Wallace et al. (2010). They found no difference in time of the DVM onset and cessation  
548 between the seasonally ice-covered and ice-free Svalbard fjords, insisting on the role of the relative change in  
549 irradiance for triggering DVM. This discrepancy highlights an important difference between sea-ice in the  
550 Svalbard fjords and the eastern Beaufort Sea continental slope. Rijpfjorden in Svalbard is seasonally ice-covered  
551 with land-fast ice of ~0.8 m thick (Wallace et al., 2010). In contrast, in spring 2015 the eastern Beaufort Sea  
552 continental slope was occupied by 2.6 m thick multi-year Greenland pack ice (Figures 3b, and 4-6) favoring the  
553 synchronized DVM to extend toward the midnight sun.

554 Our data show that, during the midnight sun 2004, DVM ceased only at 28 m depth. In the underlying  
555 PW layer at 48-108 m depth, DVM continued until the beginning of July 2004 (Figures 7c-7e). However, DVM  
556 in the PW layer did not occur in phase with the 24-h light cycle. It seems that zooplankton was conducting regular  
557 synchronized DVM, but it was still avoiding relatively well-illuminated sub-surface water. This is in line with a  
558 predator-avoidance behavior during transitional seasons, but without seasonal modulation, because the sun is  
559 above the horizon 24 h a day. In fact, zooplankton limits DVM to the PSW water layer with relatively high  
560 chlorophyll fluorescence values during late summer (Figure 2). This can indicate high concentrations of  
561 phytoplankton (e.g., La et al., 2018), which zooplankton feeds on. The availability of phytoplankton can be an  
562 important factor triggering seasonal variability in DVM (e.g., La et al., 2015).

563 Usually, synchronized DVM stops during the midnight sun, consistent with a predator-avoidance  
564 behaviour of zooplankton conducting DVM (e.g., Blachowiak-Samolyk et al., 2006; Cottier et al., 2006; Wang et  
565 al., 2015; Darnis et al., 2017). However, Fortier et al. (2001) reported a clear midnight sun DVM in copepods  
566 under the spring ice of Barrow Strait at the centre of the Canadian Arctic Archipelago. They argued that absolute  
567 light intensity below sea ice decreases to the thresholds at which the feeding activity of fish slows down.  
568 Moreover, DVM below 2-m thick ice in the Canada Basin during the midnight sun was recently reported by La  
569 et al. (2018). Following Fortier et al. (2001), we speculate that the absolute light intensity through the PW layer  
570 at CA13 was below the threshold of predators' perception allowing DVM during the midnight sun 2004. However,  
571 the midnight sun DVM was not obvious in 2005.

572 We suggest that the midnight sun DVM in 2005 was likely impacted by the enhanced concentration of  
573 suspended particles through the PSW layer. Suspended particles return the ADCP acoustic signal, producing  
574 enhanced MVBS 24 h a day. For example, Petrusевич et al. (2020) reported on enhanced MVBS in Hudson Bay  
575 recorded by 300 kHz RDI Workhorse ADCP. They attributed this signal to the suspended particles released to the  
576 water column during ice melt. In contrast to the vertically synchronized DVM, suspended particles generated  
577 noise that can mask DVM during the midnight sun 2005 as evident from Figures 7d-7f. On the CTD profile taken  
578 in September 2005, high particulate beam attenuation layers around 25 and 50 m depth match temperature maxima  
579 up to 1.3°C (Figure 2c). Moored CTD at 49 m depth shows several maxima up to 0.5°C following summer solstice  
580 2005 (Figure 9e). Two temperature maxima in the beginning and mid-June 2005 (Figure 9e) match MVBS  
581 maxima at 68-88 m depth (Figure 7f and 7g). This suggests that MVBS maxima in actograms are generated by  
582 lateral advection of warm and turbid water layers. The formation of this water is likely attributed to wind-forced



583 vertical mixing over the Beaufort Sea shelf involving surface riverine water heated by solar radiation and enriched  
584 with suspended particles. Alternatively, suspended particles can be attributed to resuspension of bottom sediments  
585 over the Beaufort Sea shelf. In any case, regardless of the source of suspended particles, their enhanced  
586 concentration in the water column during summer 2005 resulted in increased light attenuation (e.g., Hanelt et al.,  
587 2001), which potentially modified DVM during the midnight sun 2005.

## 588 **6.2 DVM modifications by moonlight**

589 In general, interpretation of the DVM modifications due to the moonlight is not straightforward. The dark-time  
590 MVBS in Figure 7c shows cumulative effect of sea-ice, cloud cover, water dynamics and moonlight. Individual  
591 events are often overlaid, and uncertainty in cloud cover also introduces an additional complication. Furthermore,  
592 during February-March, the moonlight below sea-ice is strongly attenuated (2004) or completely absorbed by sea-  
593 ice (2005) - Figure 3e. Moreover, under-ice vertical velocity data does not show DVM disruptions during full  
594 moon phases (Figure 8). However, MVBS actograms in Figures 7c-7g indicate modifications of DVM during a  
595 few days near the time of the full moon. These modifications are consistent with a lack of the upward moving  
596 zooplankton during the dark-time. They were observed from October to March including the civil twilight (Figures  
597 7b-7g). The most pronounced moonlight modifications were observed during low cloud cover periods (Figure 7).

598 While our results on the moon's modifications of DVM are not entirely conclusive, they are consistent  
599 with those previously reported for the Arctic and sub-Arctic regions. Moonlight plays a central role in structuring  
600 predator-prey interactions in the Arctic during the polar night below the ice (Last et al., 2016). It has been shown  
601 that during the polar night the moon's influence on DVM in the Arctic results in the zooplankton downward  
602 migration to deeper water for a few days near the time of the full moon (Webster et al., 2015; Last et al., 2016).  
603 This is consistent with a concept that the moon phase cycle in the zooplankton migration is a global phenomenon  
604 in the ocean as suggested by Gliwicz (1986). As to DVM, the reason for the moon's modification was  
605 hypothesized to be a predator-avoidance behaviour against predators capable of utilizing the lunar illumination.  
606 Note, however, that during civil twilight 2005 below ~1.8 m thick pack ice, zooplankton responded to the  
607 estimated lunar illumination of 0.001 lux (Figures 7b and 7c), which is far below the threshold of human and  
608 predators' perception. The moon's modification of DVM during the 2005 civil twilight suggests that zooplankton  
609 shows extraordinary sensitivity to illuminance (Båtnes et al., 2013; Cohen et al., 2015; Last et al., 2016;  
610 Petrusевич et al., 2016).

## 611 **6.3 DVM disruptions related to water dynamics**

612 Our results revealed that water dynamics temporally impact DVM by disrupting the diurnal rhythm. Upwelling  
613 affects DVM the same way as moonlight forcing zooplankton to avoid the sub-surface water layer during the dark  
614 time of the day. In contrast, downwelling seems to force zooplankton to stay in the upper intermediate water layer  
615 (consisted of PSW) for 24 h a day. During downwelling, zooplankton likely avoids the lower intermediate layer  
616 comprised by PWW. The eddy disrupts DVM in the water layer below the eddy core inverting the MVBS diurnal  
617 signal. It seems that zooplankton prevents crossing the water layer occupied by the eddy core. The general  
618 impression is that zooplankton likely avoids enhanced water dynamics.

619 The characteristic feature of high-energetic events recorded at CA13 is the depth-dependent behavior of  
620 the horizontal flow. For upwelling and downwelling over the eastern Beaufort Sea continental slope, this feature

621 is generated by the superposition of the background and wind-forced flow (Dmitrenko et al., 2018). The wind-  
622 driven barotropic flow generated by upwelling and downwelling wind forcing is superimposed on the background  
623 bottom-intensified shelfbreak current depicted by a dashed line in Figure 11c (Dmitrenko et al., 2018). For the  
624 downwelling storms, this effect amplifies the depth-intensified background circulation with enhanced PWW  
625 transport towards the Canadian Arctic Archipelago (Figure 11b and 11c, right). For the upwelling storms, the  
626 shelfbreak current is reversed, which results in surface-intensified flow moving in the opposite direction  
627 (Dmitrenko et al., 2018 and Figures 11a and 11c, left). The baroclinic eddies over the Beaufort Sea continental  
628 slope are likely explained by the shelfbreak current baroclinic instability (Spall et al., 2008).

629         It appears that upwelling, downwelling, and eddies disrupt DVM by generating a water layer with an  
630 enhanced gradient of horizontal velocity. We suggest that zooplankton avoids crossing this interface during  
631 diurnal migration, disrupting DVM. For crossing the high-gradient velocity layers, zooplankton has to spend  
632 additional energy. However, zooplankton is known for demonstrating a strategy of minimizing energy use while  
633 crossing water layers with enhanced water dynamics (Eiane et al., 1998; Basedow et al., 2004; Marcus and Scheef,  
634 2009; Petrusevich et al., 2016, 2020; Cohen and Forward, 2019). For example, Petrusevich et al. (2016) reported  
635 on the DVM deviation in an ice-covered Northeast Greenland fjord in response to the estuarine-like circulation  
636 generated by a polynya opening over the fjord mouth (Dmitrenko et al., 2015). Overall, we suggest that in addition  
637 to the predator and starvation avoidance, the zooplankton beware to cross the high-gradient velocity layers  
638 remaining behind or below them, hence disrupting DVM.

639         It is suggested that upwelling and downwelling disrupt DVM. Zooplankton is transported offshore during  
640 upwelling and shoreward during downwelling (for review see Queiroga et al., 2007). For upwelling, the wind-  
641 driven Ekman offshore transport leads to offshore dispersal and wastage from coastal habitats. This is consistent  
642 with MVBS reduction recorded in the sub-surface layer during upwelling events (Figure 7c). In fact, zooplankton  
643 can adjust migration strategy to avoid off-shore transport, reversing DVM (Poulin et al., 2002a,b). Moreover,  
644 zooplankton can avoid sweeping off-shore by upwelling and onshore by downwelling, maintaining preferred  
645 depth in the face of converging and downwelling flow (Shanks and Brink, 2005). DVM can be also impacted by  
646 the property of upwelled water. Huiwu et al. (2015) reported that DVM deviation is caused by aggregation of  
647 zooplankton in the upper 10-m layer in response to upwelling over the Chukchi Sea shelf northwest of the Alaskan  
648 coast. They explained DVM deviation by the nutrient-rich upwelled water, which favors an enhanced light  
649 attenuation by heavy phytoplankton. This, in turn, allows zooplankton to spend most of its time at the near-surface  
650 water layer.

651         We speculate that DVM disruptions attributed to upwelling and downwelling are primarily dominated  
652 by along-slope transport rather than the cross-slope transport. In addition to enhancing the cross-slope transport,  
653 upwelling and downwelling over the Beaufort Sea continental slope strongly modify along-slope transport through  
654 generating depth-dependent currents over the continental slope (Figure 11; Dmitrenko et al., 2016, 2018). We  
655 suggest that zooplankton avoids crossing horizontal velocity interface, generated by the superposition of wind-  
656 driven circulation and along-slope jet. This strategy is evident from the DVM disruption caused by the baroclinic  
657 eddy in February-March 2004. Below the depth of the maximum tangential speed (~90 m), DVM was found to  
658 be reversed (Figures 6g and 9). This is consistent with reversing DVM to avoid the upwelling induced off-shore  
659 Ekman transport in the Peru-Chile upwelling system (Poulin et al. 2002a,b). The reversed DVM in response to

660 eddy passing clearly shows that zooplankton is capable to adjust its strategy of diurnal migration to avoid enhanced  
661 water dynamics.

## 662 **7 Conclusions**

663 Based on the 2-year long time series from the mooring deployed over the upper eastern Beaufort Sea continental  
664 slope from October 2003 to September 2005, we conclude that the acoustic backscatter is dominated by DVM.  
665 DVM is controlled by the following different external forcings that also interplay.

666 (i) *Illuminance*. It is, in turn, controlled by the solar and moonlight cycling and sea-ice cover. The solar cycle  
667 controls DVM and its seasonal variability. In addition, sea-ice modifies seasonal patterns of DVM through light  
668 attenuation. A thicker multi-year Greenland pack ice present in winter-spring 2005 reduced the number of acoustic  
669 backscatters in the water column compared to that of winter-spring 2004 when the first-year pack ice dominated.  
670 Meanwhile, during spring 2005, the multi-year Greenland pack ice favored DVM prolongation toward the  
671 midnight sun due to the sea-ice shading the under-ice water layer. During civil twilight, the moon cycle generally  
672 modifies DVM, but this modification also depends on the sea-ice thickness and cloud cover. The strongest  
673 deviation was observed during mid-fall to early winter when sea ice is absent or relatively thin, and the NCEP-  
674 derived cloud cover is <30%. These deviations are associated with significant night-time reduction of acoustic  
675 backscatters in the sub-surface layer. It seems that the full moon stimulates zooplankton to avoid the sub-surface  
676 layer.

677 (ii) *Water dynamics*. Upwelling and downwelling disrupt DVM. We found that this disruption is dominated by  
678 the along-slope water dynamics rather than the cross-slope Ekman transport. The surface-intensified along-slope  
679 flow generated by upwelling drives zooplankton to the lower intermediate depths hosting PWW to avoid the sub-  
680 surface layer. Zooplankton similarly respond to upwelling as it does to the moonlight. Thus, DVM disruptions  
681 induced by upwelling often interferes with the one generated by moonlight. In contrast, the bottom-intensified  
682 along-slope flow generated by downwelling modifies DVM through accumulating zooplankton in the upper  
683 intermediate layer occupied by PSW. The baroclinic eddy reverses DVM below the eddy core. We suggest that  
684 the zooplankton's response to upwelling, downwelling, and eddy is consistent with adjusting DVM to avoid  
685 enhanced water dynamics.

686 In contrast to many previous studies of the high-Arctic regions, at ~71°N latitude we recorded DVM  
687 during the midnight sun. During the ice-free season of the midnight sun 2004, DVM was observed through the  
688 PW layer. This DVM is likely limited by the depth of chlorophyll maxima in PSW. In 2005 the midnight sun  
689 DVM seemed to be masked by a high acoustic scattering level attributed to warmer and turbid layers observed  
690 through PSW.

691 Our analysis was limited by deficient zooplankton observations. A comprehensive analysis of the  
692 scattering species comprising DVM is logistically impossible for the long-term deployments in the seasonally ice-  
693 covered and remote areas in the high Arctic. This prohibits identification of specific species whose DVM was  
694 detected by the 300 kHz ADCP and altered by the different environmental factors including illuminance and water  
695 dynamics.

696 **Acknowledgments**

697 We appreciate Jørgen Berge from the Arctic University of Norway and another anonymous reviewer for their  
698 constrictive comments and suggestions. The data used for this research were collected under the ArcticNet  
699 framework, project Long-Term Oceanic Observatories in the Canadian Arctic. We gratefully acknowledge the  
700 support by the Canada Excellence Research Chair (CERC) and the Canada Research Chairs (CRC) programs.  
701 This work is a contribution to the joint Canadian-Danish-Greenland Arctic Science Partnership, Québec-Ocean,  
702 and the Canada Research Chair on the response of Arctic marine ecosystems to climate warming. The research  
703 was also partly supported by the National Sciences and Engineering Research Council of Canada (IAD: grant  
704 RGPIN-2014-03606, JKE: grant RGPIN/435373-2013).

705 **Data**

706 The ADCP data are available through the Polar Data Catalogue at <https://www.polardata.ca/pdcsearch/>, CCIN  
707 Reference #11653 (Gratton et al., unpublished).

708 **Authors' contributions**

709 Contributed to conception and design: IAD, VP, GD, SR, DB  
710 Contributed to acquisition of data: JKE, AK, GD, AF, LF  
711 Contributed to analysis and interpretation of data: IAD, VP, AK, GD, SK  
712 Drafted and/or revised the article: IAD, VP, AK, GD, SR  
713 Approved the submitted version for publication: IAD

714 **References**

715 Barber, D.G, Hop, H., Mundy, C.J., Else, B., Dmitrenko, I.A., Tremblay, J.-E., Ehn, J.K., Assmy, P., Daase, M.,  
716 Candlish, L.M., and Rysgaard, S.: Selected physical, biological and biogeochemical implications of a rapidly  
717 changing Arctic Marginal Ice Zone, *Prog. Oceanogr.*, 139, 122–150, doi:10.1016/j.pocean.2015.09.003, 2015.  
718 Basedow, S., Eiane, K., Tverberg, V. and Spindler, M.: Advection of the zooplankton in an Arctic fjord  
719 (Kongsfjorden, Svalbard), *Estuarine Coastal Shelf Sci.*, 60(1), 113–124, doi:10.1016/j.ecss.2003.12.004, 2004.  
720 Båtnes, A. S., Miljeteig, C., Berge, J., Greenacre, M., and Johnsen, G.: Quantifying the light sensitivity of *Calanus*  
721 spp. during the polar night: potential for orchestrated migrations conducted by ambient light from the sun, moon,  
722 or aurora borealis?, *Polar Biol.*, 1, 15, doi: 10.1007/s00300-013-1415-4, 2013.  
723 Berge, J., Renaud, P.E., Darnis, G., Cottier, F., Last, K., Gabrielsen, T.M., Johnsen, G., Seuthe, L., Weslawski,  
724 J.M., Leuc, E., Moline, M., Nahrgang, J., Søreide, J.E., Varpeb, Ø., Lønne, O.J., Daasea, M., and Falk-Petersen,  
725 S.: In the dark: A review of ecosystem processes during the Arctic polar night, *Prog. Oceanogr.*, 139, 258–271,  
726 doi:10.1016/j.pocean.2015.08.005, 2015.  
727 Berge J., Cottier, F., Last, K.S., Varpe, Ø., Leu, E., Søreide, J., Eiane, K., Falk-Petersen, S., Willis, K., Nygård,  
728 H., Vogedes, D., Griffiths, C., Johnsen, G., Lorentzen, D., and Brierley, A.S., Diel vertical migration of Arctic  
729 the zooplankton during the polar night, *Biol. Lett.*, 5, 69–72, doi: 10.1098/rsbl.2008.0484, 2009.

730 Brierley, A.S., Brandon, M.A., and Watkins, J.L., An assessment of the utility of an acoustic Doppler current  
731 profiler for biomass estimation, *Deep Sea Res. Part I*, 45(9), 1555–1573, doi: 10.1016/S0967-0637(98)00012-0,  
732 1998.

733 Brierley, A.S., Diel vertical migration, *Curr. Biol.*, 24, R1074–R1076, doi: 10.1016/j.cub.2014.08.054, 2014.

734 Chassignet, E.P., Hurlburt, H.E., Smedstad, O.M., Halliwell, G.R., Hogan, P.J., Wallcraft, A.J., Baraille, R., and  
735 Bleck, R., The HYCOM (Hybrid Coordinate Ocean Model) data assimilative system, *Journal of Marine Systems*,  
736 65, 60–83, doi: 10.1016/j.jmarsys.2005.09.016, 2007.

737 Cohen, J.H., Berge, J., Moline, M.A., Sørensen, A.J., Last, K., Falk-Petersen, S., Renaud, P.E., Leu, E.S.,  
738 Grenvald, J., Cottier, F., Cronin, H., Menze, S., Norgren, P., Varpe, Ø., Daase, M., Darnis, G., and Johnsen, G.,  
739 Is Ambient Light during the High Arctic Polar Night Sufficient to Act as a Visual Cue for Zooplankton?, *PLoS*  
740 *ONE*, 10(6), e0126247, doi: 10.1371/journal.pone.0126247, 2015.

741 Cavalieri, D.J., Markus, T., and Comiso, J.C., AMSR-E/Aqua Daily L3 12.5 km Brightness Temperature, Sea Ice  
742 Concentration, & Snow Depth Polar Grids, Version 3. Boulder, Colorado USA. NASA National Snow and Ice  
743 Data Center Distributed Active Archive Center, doi: 10.5067/AMSR-E/AE\_SII2.003, 2014.

744 Cohen, J.H., and Forward, R.B., Zooplankton Diel Vertical Migration - A Review Of Proximate Control,  
745 *Oceanography and marine biology: An Annual Review*, 47, 77-109, 2009.

746 Cohen, J.H., and Forward, R.B., Vertical Migration of Aquatic Animals, *Encyclopedia of Animal Behavior*  
747 (Second Edition), Elsevier, 546-552, doi: 10.1016/B978-0-12-809633-8.01257-7, 2019.

748 Cottier F.R., Tarling, G.A., Wold, A., and Falk-Petersen, S., Unsynchronised and synchronised vertical migration  
749 of the zooplankton in a high Arctic fjord, *Limnol. Oceanogr.*, 51, 2586–2599, doi: 10.4319/lo.2006.51.6.2586,  
750 2006.

751 Darnis, G., Hobbs, L., Geoffroy, M., Grenvald, J.C., Renaud, P.E., Berge, J., Cottier, F., Kristiansen, S., Daase,  
752 M., Søreide, J.E., Wold, A., Morata, N., and Gabrielsen, T., From polar night to midnight sun: Diel vertical  
753 migration, metabolism and biogeochemical role of the zooplankton in a high Arctic fjord (Kongsfjorden,  
754 Svalbard), *Limnol. Oceanogr.*, 62, 1586–1605, doi: 10.1002/lno.10519, 2017.

755 Deines, K.L., Backscatter estimation using Broadband acoustic Doppler current profilers, in *Proceedings of the*  
756 *IEEE Sixth Working Conference on Current Measurement (Cat. No.99CH36331)*, pp. 249–253, IEEE, San Diego,  
757 Calif, 1999.

758 Dmitrenko, I.A., Kirillov, S.A., Myers, P.G., Forest, A., Tremblay, B., Lukovich, J.V., Gratton, Y., Rysgaard, S.,  
759 and Barber, D.G., Wind-forced depth-dependent currents over the eastern Beaufort Sea continental slope:  
760 Implications for Pacific water transport, *Elem. Sci. Anth.*, 6, 66, doi: 10.1525/elementa.321, 2018.

761 Dmitrenko, I.A., Kirillov, S.A., Forest, A., Gratton, Y., Volkov, D.L., Williams, W.J., Lukovich, J.V., Belanger,  
762 C., and Barber, D.G., Shelfbreak current over the Canadian Beaufort Sea continental slope: Wind-driven events  
763 in January 2005, *J. Geophys. Res.*, 121(4), 2447-2468, doi: 10.1002/2015JC011514, 2016.

764 Dmitrenko, I.A., Kirillov, S.A., Rysgaard, S., Barber, D.G., Babb, D.G., Pedersen, L.T., Koldunov, N.V., Boone,  
765 W., Crabeck, O., and Mortensen, J., Polynya impacts on water properties in a Northeast Greenland Fjord,  
766 *Estuarine Coastal Shelf Sci.*, 153, 10–17, doi:10.1016/j.ecss.2014.11.027, 2015,

767 Dmitrenko, I.A., Wegner, C., Kassens, H., Kirillov, S.A., Krumpfen, T., Heinemann, G., Helbig, A., Schröder, D.,  
768 Hölemann, J.A., Klagge, T., Tyshko, K.P., and Busche, T., Observations of supercooling and frazil ice formation  
769 in the Laptev Sea coastal polynya, *J. Geophys. Res.*, 115, C05015, doi: 10.1029/2009JC005798, 2010.

770 Dmitrenko, I.A., Kirillov, S.A., Ivanov, V.V., and Woodgate, R.A., Mesoscale Atlantic water eddy off the Laptev  
771 Sea continental slope carries the signature of upstream interaction, *J. Geophys. Res.*, 113, C07005, doi:  
772 10.1029/2007JC004491, 2008.

773 Eiane, K., Aksnes, D., and Ohman, M., Advection and the zooplankton fitness, *SARSIA*, 83, 87–93, doi:  
774 10.1080/00364827.1998.10413674, 1998.

775 Falk-Petersen, S., Leu, E., Berge, J., Kwasniewski, S., Nygård, H., Røstad, A., Keskinen, E., Thormar, J.,  
776 Quillfeldt, C., Wold, A., and Gulliksen, B., Vertical migration in high Arctic waters during autumn 2004, *Deep*  
777 *Sea Res., Part II*, 55(20-21), 2275–2284, doi: 10.1016/j.dsr2.2008.05.010, 2008.

778 Fielding, S., Griffiths, G., and Roe, H.S.J., The biological validation of ADCP acoustic backscatter through direct  
779 comparison with net samples and model predictions based on acoustic-scattering models, *ICES J. Mar. Sci. J. du*  
780 *Cons.*, 61(2), 184–200, doi: 10.1016/j.icesjms.2003.10.011, 2004.

781 Fortier, M., Fortier, L., Hattori, H., Saito, H., and Legendre, L., Visual predators and the diel vertical migration  
782 of copepods under Arctic sea ice during the midnight sun, *J. Plankton Res.*, 23, 1263–1278, doi:  
783 10.1093/plankt/23.11.1263, 2001.

784 Gaston, K.J., Duffy, J.P., Gaston, S., Bennie, J., and Davies, T.W., Human alteration of natural light cycles: causes  
785 and ecological consequences, *Oecologia*, 176, 917–931, doi: 10.1007/s00442-014-3088-2, 2014.

786 Gliwicz, Z.M., A Lunar Cycle in The Zooplankton, *Ecology*, 67(4), 883-897, doi: 10.2307/1939811, 1986.

787 Gratton, Y., Ingram, G., Carmack, E., Van Hardenberger, B., Forest, A., Fortier, L., Blondeau, S., Massot, P., and  
788 Michaud, L., Long-term oceanic observatories (moorings) in the Beaufort Sea during the Canadian Arctic Shelf  
789 Exchange Study, 2002–2004, doi: 10.5884/11653, unpublished.

790 Grenfell, C.G., and Maykut, G.A., The optical properties of ice and snow in the Arctic Basin, *J. Glaciol.*, 18(80),  
791 445–463, doi: 10.3189/S0022143000021122, 1977.

792 Grenvald, J.C., Callesen, T.A., Daase, M., Hobbs, L., Darnis, G., Renaud, P.E., Cottier, F., Nielsen, T.G., and  
793 Berge, J., Plankton community composition and vertical migration during polar night in Kongsfjorden, *Polar*  
794 *Biology*, 39, 1879–1895, doi: 10.1007/s00300-016-2015-x, 2016.

795 Hanelt, D., Tüg, H., Bischof, K., Groß, C., Lippert, H., Sawall, T., and Wiencke, C., Light regime in an Arctic  
796 fjord: a study related to stratospheric ozone depletion as a basis for determination of UV effects on algal growth,  
797 *Marine Biology*, 138(3), 649–658, doi: 10.1007/s002270000481, 2001.

798 Hays G.C., A review of the adaptive significance and ecosystem consequences of the zooplankton diel vertical  
799 migrations, *Hydrobiologia*, 503, 163–170, doi: 10.1023/B:HYDR.0000008476.23617.b0, 2003.

800 Hobbs, L., Cottier, F.R., Last, K.S., and Berge, J., Pan-Arctic diel vertical migration during the polar night, *Mar.*  
801 *Ecol. Prog. Ser.*, 605, 61– 72, doi: 10.3354/meps12753, 2018.

802 Hunke, E.C., Viscous-plastic sea ice dynamics with the EVP model: linearization issues, *Computational*  
803 *Physics*, 170, 18–38, doi: 10.1006/jcph.2001.6710, 2001.

804 Kalnay, E., et al., The NCEP/NCAR 40-year reanalysis project, *Bull. Am. Meteorol. Soc.*, 77, 437–471, doi:  
805 10.1175/1520-0477(1996)077<0437:TNYRP>2.0.CO;2, 1996.

806 Kirillov, S., Dmitrenko, I., Tremblay, B., Gratton, Y., Barber, D., and Rysgaard, S., Upwelling of Atlantic Water  
807 along the Canadian Beaufort Sea continental slope: Favorable atmospheric conditions and seasonal and  
808 interannual variations, *J. Climate*, 29(12), 4509–4523, doi: 10.1175/JCLI-D-15-0804.1, 2016.

809 Kosobokova, K.N., Diurnal vertical distribution of *Calanus Hyperboreus* Kroyer and *Calanus Glacialis* Jaschnov  
810 in Central Polar Basin, *Okeanologiya*, 18(4), 722–728, 1978.

811 Krishfield, R.A., Proshutinsky, A., Tateyama, K., Williams, W.J., Carmack, E.C., McLaughlin, F.A., and  
812 Timmermans, M.-L., Deterioration of perennial sea ice in the Beaufort Gyre from 2003 to 2012 and its impact on  
813 the oceanic freshwater cycle, *J. Geophys. Res. Oceans*, 119, 1271–1305, doi: 10.1002/2013JC008999, 2014.

814 Kulikov, E.A., Carmack, E.C., and Macdonald, R.W., Flow variability at the continental shelf break of the  
815 Mackenzie Shelf in the Beaufort Sea, *J. Geophys. Res.*, 103(C6), 12,725–12,741, doi: 10.1029/97JC03690, 1998.

816 Kwok, R., Cunningham, G.F., Zwally, H.J., and Yi, D., Ice, Cloud, and land Elevation Satellite (ICESat) over  
817 Arctic sea ice: Retrieval of freeboard, *J. Geophys. Res.*, 112, C12013, doi: 10.1029/2006JC003978, 2007.

818 Kwok, R., Cunningham, G.F., Wensnahan, M., Rigor, I., Zwally, H.J., and Yi, D., Thinning and volume loss of  
819 the Arctic Ocean sea ice cover: 2003–2008, *J. Geophys. Res.*, 114, C07005, doi: 10.1029/2009JC005312, 2009.

820 La, H.S., Shimada, K., Yang, E.J., Cho, K.-H., Ha, S.-Y., Jung, J., Min, J.-O., Kang, S.-H., and Ha, H.K., Further  
821 evidence of diel vertical migration of copepods under Arctic sea ice during summer, *Mar. Ecol. Prog. Ser.*, 592,  
822 283–289, doi: 10.3354/meps12484, 2018.

823 La, H.S., Ha, H.K., Kang, C.Y., Wåhlin, A.K., and Shin, H.C., Acoustic backscatter observations with  
824 implications for seasonal and vertical migrations of the zooplankton and nekton in the Amundsen shelf  
825 (Antarctica), *Estuarine, Coastal and Shelf Sci.*, 152, 124–133, doi: 10.1016/j.ecss.2014.11.020, 2015.

826 Last, K.S., Hobbs, L., Berge, J., Brierley, A.S., and Cottier, F., Moonlight drives ocean-scale mass vertical  
827 migration of the zooplankton during the Arctic Winter, *Curr. Biol.*, 26(2), 244–251, doi:  
828 10.1016/j.cub.2015.11.038, 2016.

829 Leise, T.L., Indic, P., Paul, M.J., and Schwartz, W.J., Wavelet meets actogram, *J. Biol. Rhythms*, 28(1), 62–68,  
830 doi: 10.1177/0748730412468693, 2013.

831 Lemon, D.D., Gower, J.F.R., and Clarke, M.R., The acoustic water column profiler: a tool for long-term  
832 monitoring of zooplankton populations, In: *MTS/IEEE Oceans 2001. An Ocean Odyssey*, Conference  
833 Proceedings (IEEE Cat. No.01CH37295), Honolulu, HI, USA, pp. 1904–1909, vol.3, doi:  
834 10.1109/OCEANS.2001.968137, 2001.

835 Lemon, D.D., Billenness, D., and Buermans, J., Comparison of acoustic measurements of zooplankton  
836 populations using an Acoustic Water Column Profiler and an ADCP, In: *OCEANS 2008*, Quebec City, QC, pp.  
837 1–8, doi: 10.1109/OCEANS.2008.5152009, 2008.

838 Lemon, D., Johnston, P., Buermans, J., Loos, E., Borstad, G., and Brown, L., Multiple-frequency moored sonar  
839 for continuous observations of zooplankton and fish, In: *2012 Oceans*, Hampton Roads, VA, pp. 1–6, doi:  
840 10.1109/OCEANS.2012.6404918, 2012.

841 Liu, Y., and Key, J.R., Assessment of Arctic Cloud Cover Anomalies in Atmospheric Reanalysis Products Using  
842 Satellite Data, *J. Climate*, 29, 6065–6083, doi: 10.1175/JCLI-D-15-0861.1, 2016.

843 Lorke, A., McGinnis, D.F., Spaak, P., and Wüest, A., Acoustic observations of zooplankton in lakes using a  
844 Doppler current profiler, *Freshw. Biol.*, 49, 1280–1292, doi: 10.1111/j.1365-2427.2004.01267.x, 2004.

845 Marcus, N.H., and Scheef, L.P., Photoperiodism in Copepods, in *Photoperiodism: The Biological Calendar*, edited  
846 by Nelson, R.J., Denlinger, D.L., and Sommers, D.E., pp. 193–217, Oxford University Press, Oxford, U. K., 2009.

847 Madsen, K.S., Rasmussen, T.A.S., Ribergaard, M.H., and Ringgaard, I.M., High resolution sea ice modelling and  
848 validation of the Arctic with focus on south Greenland waters, 2004-2013, *Polarforschung*, 85(2), 101-105, doi:  
849 10.2312/polfor.2016.006, 2015.

850 Markus, T. and Cavalieri, D., Snow Depth Distribution over Sea Ice in the Southern Ocean from Satellite Passive  
851 Microwave Data. In: *Antarctic Sea Ice: Physical Processes, Interactions, and Variability*, Antarctic Research  
852 Series, 74, 19-39. Washington, DC: American Geophysical Union, 1998.

853 Melling, H., Riedel, D.A., and Gedalof, Z., Trends in the draft and extent of seasonal pack ice, Canadian Beaufort  
854 Sea, *Geophys. Res. Lett.*, 32, L24501, doi:10.1029/2005GL024483, 2005.

855 O'Brien, M.C., Melling, H., Pedersen, T.F., and Macdonald, R.W., The role of eddies and energetic ocean  
856 phenomena in the transport of sediment from shelf to basin in the Arctic, *J. Geophys. Res.*, 116, C08001, doi:  
857 10.1029/2010JC006890, 2011.

858 Ott, M.J., The accuracy of acoustic vertical velocity measurements: instrument biases and the effect of  
859 Zooplankton migration, *Continental Shelf Research*, 25, 243-257, doi: 10.1016/j.csr.2004.09.007, 2005.

860 Perovich, D.K., The optical properties of sea ice, *CRREL Monogr.*, 96-1, 25, 1996.

861 Petrushevich, V.Y., Dmitrenko, I.A., Niemi, A., Kirillov, S.A., Kamula, C.M., Kuzyk, Z.Z.A., Barber, D.G., and  
862 Ehn, J.K., Impact of tidal dynamics on diel vertical migration of zooplankton in Hudson Bay, *Ocean Science*, 16,  
863 337-353, doi: 10.5194/os-16-337-2020, 2020.

864 Petrushevich, V., Dmitrenko, I.A., Kirillov, S.A., Rysgaard, S., Falk-Petersen, S., Barber, D.G., Boone, W., and  
865 Ehn, J.K., Wintertime water dynamics and moonlight disruption of the acoustic backscatter diurnal signal in an  
866 ice-covered Northeast Greenland fjord, *J. Geophys. Res. Oceans*, 121, 4804-4818, doi: 10.1002/2016JC011703,  
867 2016.

868 Pickart, R.S., Shelfbreak circulation in the Alaskan Beaufort Sea: Mean structure and variability, *J. Geophys.*  
869 *Res.*, 109, C04024, doi: 10.1029/2003JC001912, 2004.

870 Pickart, R.S., Weingartner, T.J., Pratt, L.J., Zimmermann, S., and Torres, D.J., Flow of winter-transformed Pacific  
871 water into the western Arctic, *Deep Sea Res., Part II*, 52, 3175-3198, doi: 10.1016/j.dsr2.2005.10.009, 2005.

872 Pnyushkov, A., Polyakov, I.V., Padman, L., and Nguyen, A.T., Structure and dynamics of mesoscale eddies over  
873 the Laptev Sea continental slope in the Arctic Ocean, *Ocean Sci.*, 14, 1329-1347, doi: 10.5194/os-14-1329-2018,  
874 2018.

875 Poulin, E., Palma, A.T., Leiva, G., Narvaez, D., Pacheco, R., Navarrete, S.A., and Castilla, J.C., Avoiding offshore  
876 transport of competent larvae during upwelling events: The case of the gastropod *Concholepas concholepas* in  
877 Central Chile, *Limnol. Oceanogr.*, 47(4), 1248-1255, doi: 10.4319/lo.2002.47.4.1248, 2002a.

878 Poulin, E., Palma, A.T., Leiva, G., Hernández, E., Martínez, P., Navarrete, S.A., and Castilla, J.C., Temporal and  
879 spatial variation in the distribution of epineustonic competent larvae of *Concholepas concholepas* along the central  
880 coast of Chile, *Mar. Ecol. Prog. Ser.*, 229, 95-104, doi: 0.3354/meps229095, 2002b.

881 Queiroga, H., Cruz, T., dos Santos, A., Dubert, J., Gonzalez-Gordillo, J.I., Paula, J., Peliz, A., and Santos, A.M.P.,  
882 Oceanographic and behavioural processes affecting invertebrate larval dispersal and supply in the western Iberia  
883 upwelling ecosystem, *Progress in Oceanography*, 74, 174-19, doi: 10.1016/j.pocean.2007.04.007, 2007.

884 Shanks, A.L., and Brink, L., Upwelling, downwelling, and cross-shelf transport of bivalve larvae: test of a  
885 hypothesis, *Mar. Ecol. Prog. Ser.*, 302: 1-12, doi: 10.3354/meps302001, 2005.



886 Spreen, G., Kaleschke, L., and Heygster, G., Sea ice remote sensing using AMSR-E 89 GHz channels, *J. Geophys.*  
887 *Res.*, 113, C02S03, doi: 10.1029/2005JC003384, 2008.

888 Schweiger, A., Lindsay, R., Zhang, J., Steele, M., Stern, H., Uncertainty in modeled arctic sea ice volume, *J.*  
889 *Geophys. Res.*, doi: 10.1029/2011JC007084, 2011

890 Spall, M., Pickart, R., Fratantoni, P., and Plueddemann, A., Western Arctic shelfbreak eddies: Formation and  
891 transport, *J. Phys. Oceanogr.*, 38, 1644–1668, doi: 10.1175/2007JPO3829.1, 2008.

892 Stanton, T.K., Wiebe, P.H., Chu, D., Benfield, M.C., Scanlon, L., Martin, L., and Eastwood, R.L., On acoustic  
893 estimates of zooplankton biomass, *ICES J. Mar. Sci.*, 51(4), 505–512, doi: 10.1006/jmsc.1994.1051, 1994.

894 Sun H., Hendry, D.C., Player, M.A. and Watson, J., In Situ Underwater Electronic Holographic Camera for  
895 Studies of Plankton, *IEEE Journal of Oceanic Engineering*, 32(2), 373–382, doi: 10.1109/JOE.2007.891891,  
896 2007.

897 Tran, D., Sow, M., Camus, L., Ciret, P., Berge, J., and Massabuau, J.-C., In the darkness of the polar night, scallops  
898 keep on a steady rhythm, *Sci. Reports*, 6, 32435, doi: 10.1038/srep32435, 2016.

899 van Haren, H., and Compton, T.J., Diel Vertical Migration in Deep Sea Plankton Is Finely Tuned to Latitudinal  
900 and Seasonal Day Length, *PLoS One*, 8(5), e64435, doi: 10.1371/journal.pone.0064435, 2013.

901 Vestheim, H., Røstad, A., Klevjer, T.A., Solberg, I., and Kaartvedt, S., Vertical distribution and diel vertical  
902 migration of krill beneath snow-covered ice and in ice-free waters, *J. Plankton Res.*, 36(2), 503–512, doi:  
903 10.1093/plankt/fbt112, 2014.

904 Wallace, M.I., Cottier, F.R., Berge, J., Tarling, G.A., Griffiths, C., and Brierley, A.S., Comparison of the  
905 zooplankton vertical migration in an ice-free and a seasonally ice-covered Arctic fjord: An insight into the  
906 influence of sea ice cover on the zooplankton behavior, *Limnol. Oceanogr.*, 55(2), 831–845, doi:  
907 10.4319/lo.2010.55.2.0831, 2010.

908 Wang, H., Chen, H., Xue, L., Liu, N., and Liu, Y., The zooplankton diel vertical migration and influence of  
909 upwelling on the biomass in the Chukchi Sea during summer, *Acta Oceanologica Sinica*, 34(5), 68–74, doi:  
910 10.1007/s13131-015-0668-x, 2015.

911 Wang, X., Key, J., Kwok, R., and Zhang, J., Comparison of Arctic Sea Ice Thickness from Satellites, Aircraft,  
912 and PIOMAS Data, *Remote Sens.*, 8, 713, doi: 10.3390/rs8090713, 2016.

913 Webster, C., Varpe, Ø., Falk-Petersen, S., Berge, J., Stübner, E., and Brierley, A., Moonlit swimming: Vertical  
914 distributions of macrothe zooplankton and nekton during the polar night, *Polar Biol.*, 38(1), 75–85, doi:  
915 10.1007/s00300-013-1422-5, 2015.

916 Weingartner, T., Cavalieri, D., Aagaard, K., and Sasaki, Y., Circulation, dense water formation, and outflow on  
917 the northeast Chukchi shelf, *J. Geophys. Res.*, 103(C4), 7647–7661, doi: 10.1029/98JC00374, 1998.

918 Williams, W.J., Carmack, E.C., Shimada, K., Melling, H., Aagaard, K., Macdonald, R.W., and Ingram, R.G., Joint  
919 effects of wind and ice motion in forcing upwelling in Mackenzie Trough, Beaufort Sea, *Cont. Shelf Res.*, 26,  
920 2352–2366, doi: 10.1016/j.csr.2006.06.012, 2006.

921 Wood, T.M., and Gartner, J.W., Use of Acoustic Backscatter and Vertical Velocity to Estimate Concentration and  
922 Dynamics of Suspended Solids in Upper Klamath Lake, South-Central Oregon: Implications for Aphanizomenon  
923 flos-aquae, *Scientific Investigations Report 2010–5203*, U.S. Geological Survey, Reston, Virginia, 20 p., 2010.

924 Woodgate, R.A., Aagaard, K., and Weingartner, T.J., Monthly temperature, salinity, and transport variability of  
925 the Bering Strait through flow, *Geophys. Res. Lett.*, 32, L04601, doi: 10.1029/2004GL021880, 2005.

926 Yi, D., and Zwally, H.J., Arctic Sea Ice Freeboard and Thickness, Version 1. Boulder, Colorado USA. NASA  
927 National Snow and Ice Data Center Distributed Active Archive Center, doi: 10.5067/SXJVJ3A2XIZT. 2009,  
928 updated 2014.

929 Zhang, J.L. and Rothrock, D.A., Modeling global sea ice with a thickness and enthalpy distribution model in  
930 generalized curvilinear coordinates“, Mon. Weather Rev., 131, 845-861, doi: 10.1175/1520-  
931 0493(2003)131<0845:MGSIWA>2.0.CO;2, 2003.

932

933 **Figures**

934

935

936

937

938

939

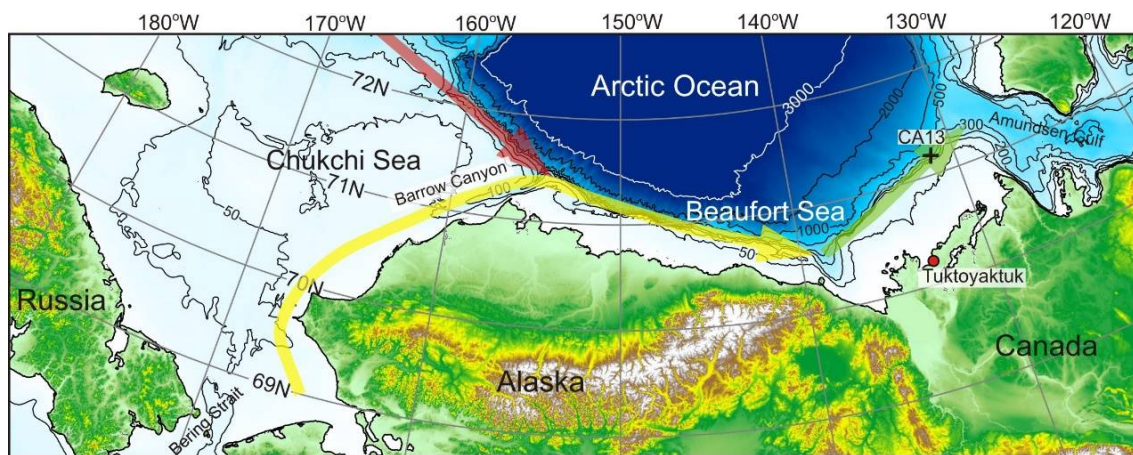
940

941

942

943

944

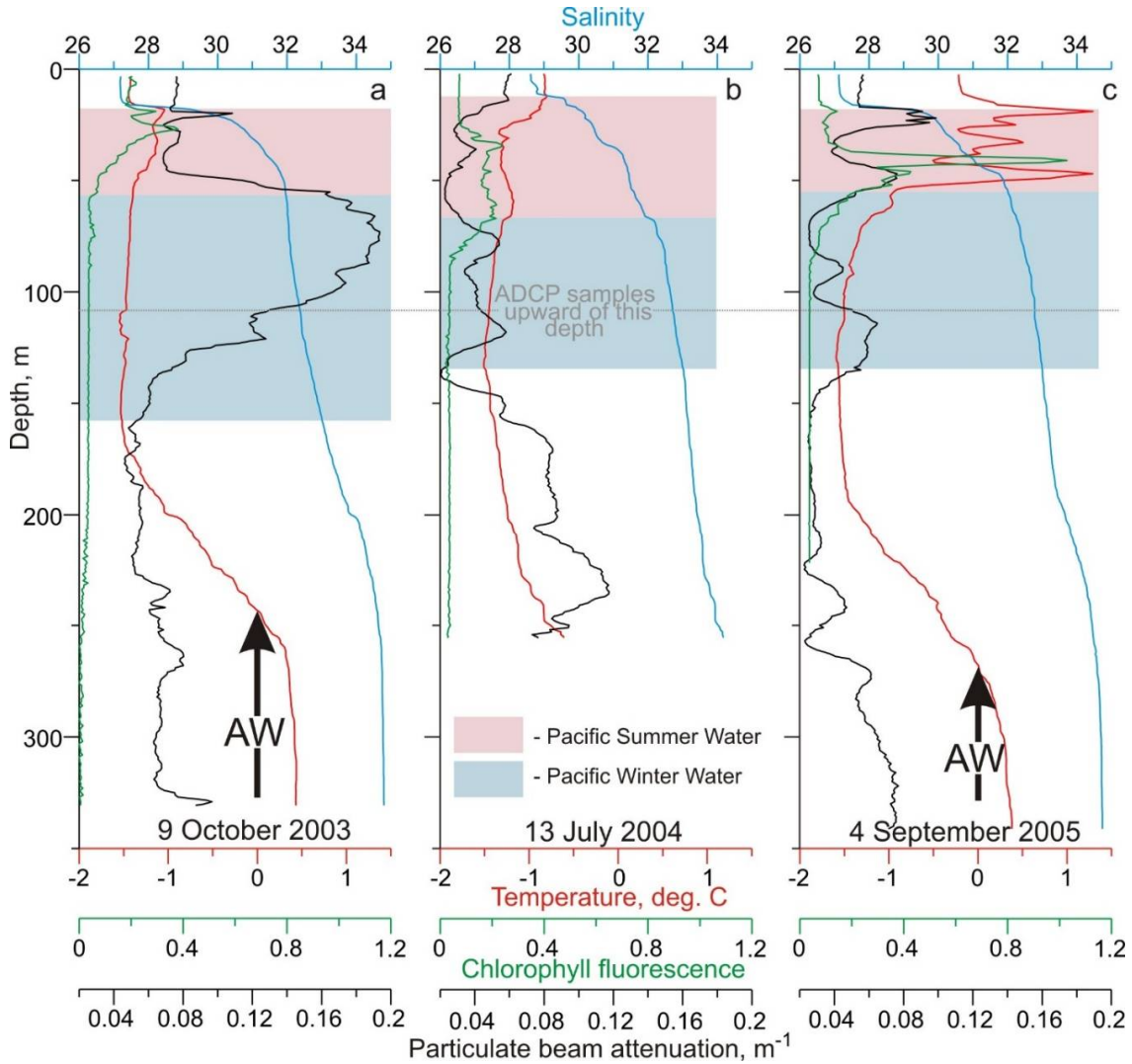


945

946 **Figure 1:** Map of the Beaufort Sea with the location of the ArcticNet mooring CA13 (black  
947 numbered cross). Thick red, yellow, and green arrows show circulation associated with the  
948 shelfbreak jet over the Chukchi Sea and western and eastern Beaufort Sea, respectively.

949

950  
951  
952



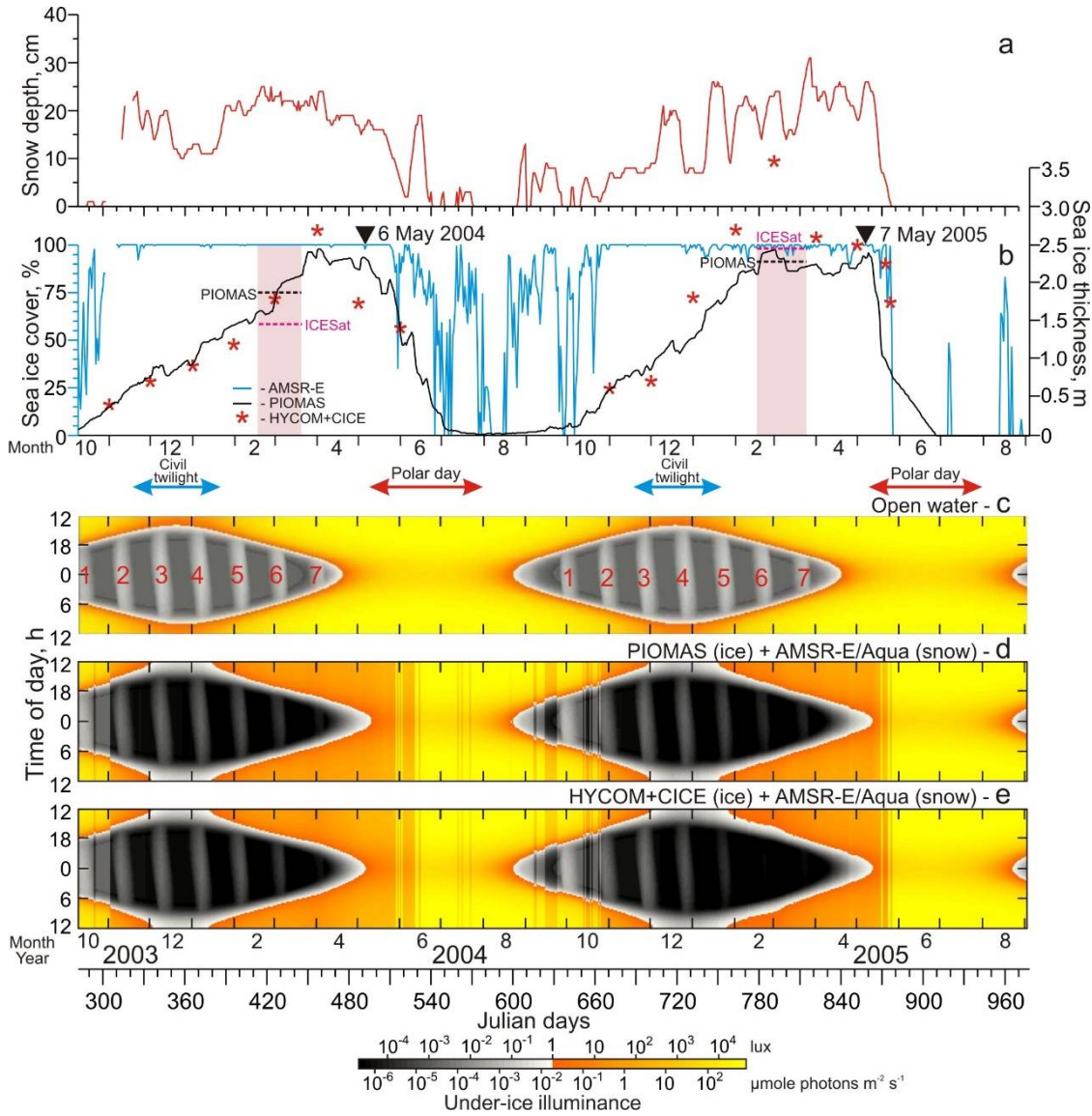
953

954 **Figure 2:** Vertical temperature (red), salinity (blue), chlorophyll fluorescence (green) and  
955 particulate beam attenuation (black) profiles taken at (a) mooring deployment on 9 October  
956 2003, (b) on 13 July 2004 and (c) at mooring recovery on 4 September 2005. Pink and blue  
957 shading and black arrows highlight Pacific Summer Water (PSW), Pacific Winter Water  
958 (PWW), and Atlantic Water (AW), respectively, following Dmitrenko et al. (2016).

959

960

961

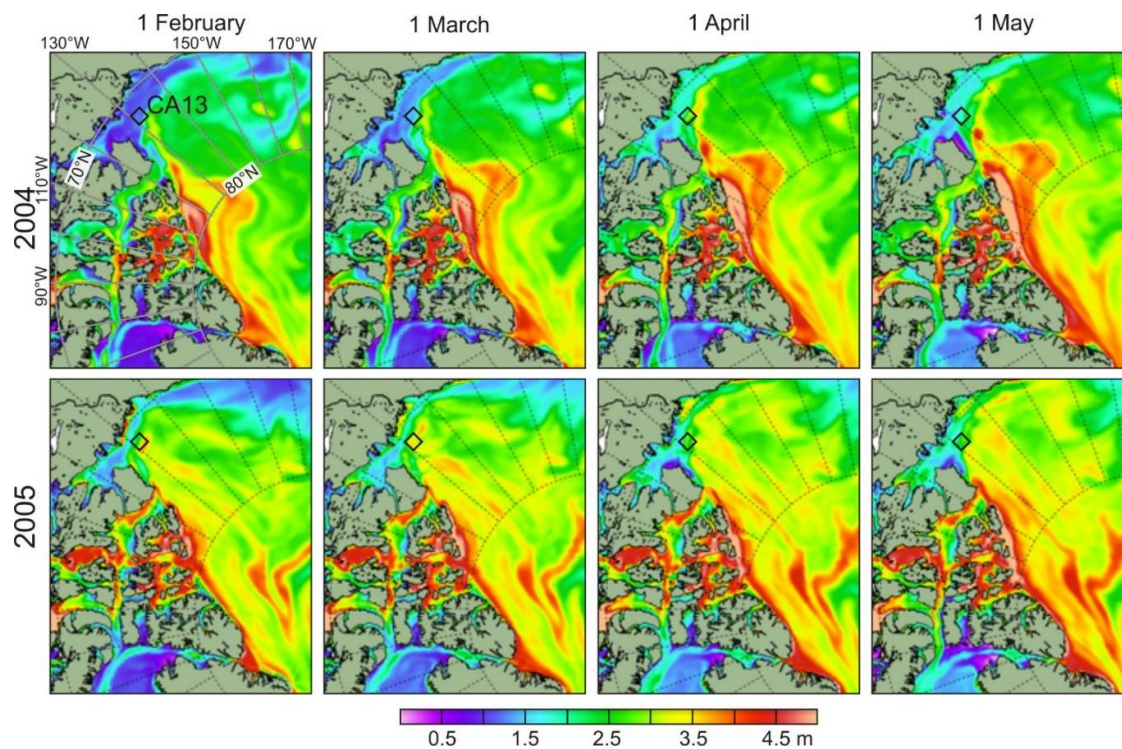


962

963 **Figure 3:** Time series of the (a) snow depth (cm, red), and (b) sea-ice concentrations (%) and thickness (m) from PIOMAS (black) and HYCOM+CICE (red stars). (b) Pink shading highlights periods of two ICESat campaigns. Black and purple horizontal segments indicate the mean sea-ice thickness derived from PIOMAS and ICESat, respectively. Black triangles at the top identify the time when the RADARSAT satellite images in Figure 6 were acquired. (c-e) Actograms of under-ice illuminance modeled for (c) open water conditions, (d,e) snow from AMSR-E/Aqua, and sea-ice thickness from (d) PIOMAS and (e) HYCOM+CICE. Red and blue arrows at the top indicate the polar day and civil twilight, respectively. (c) Red numbers reference the full moon occurrences.



972  
973  
974  
975  
976  
977

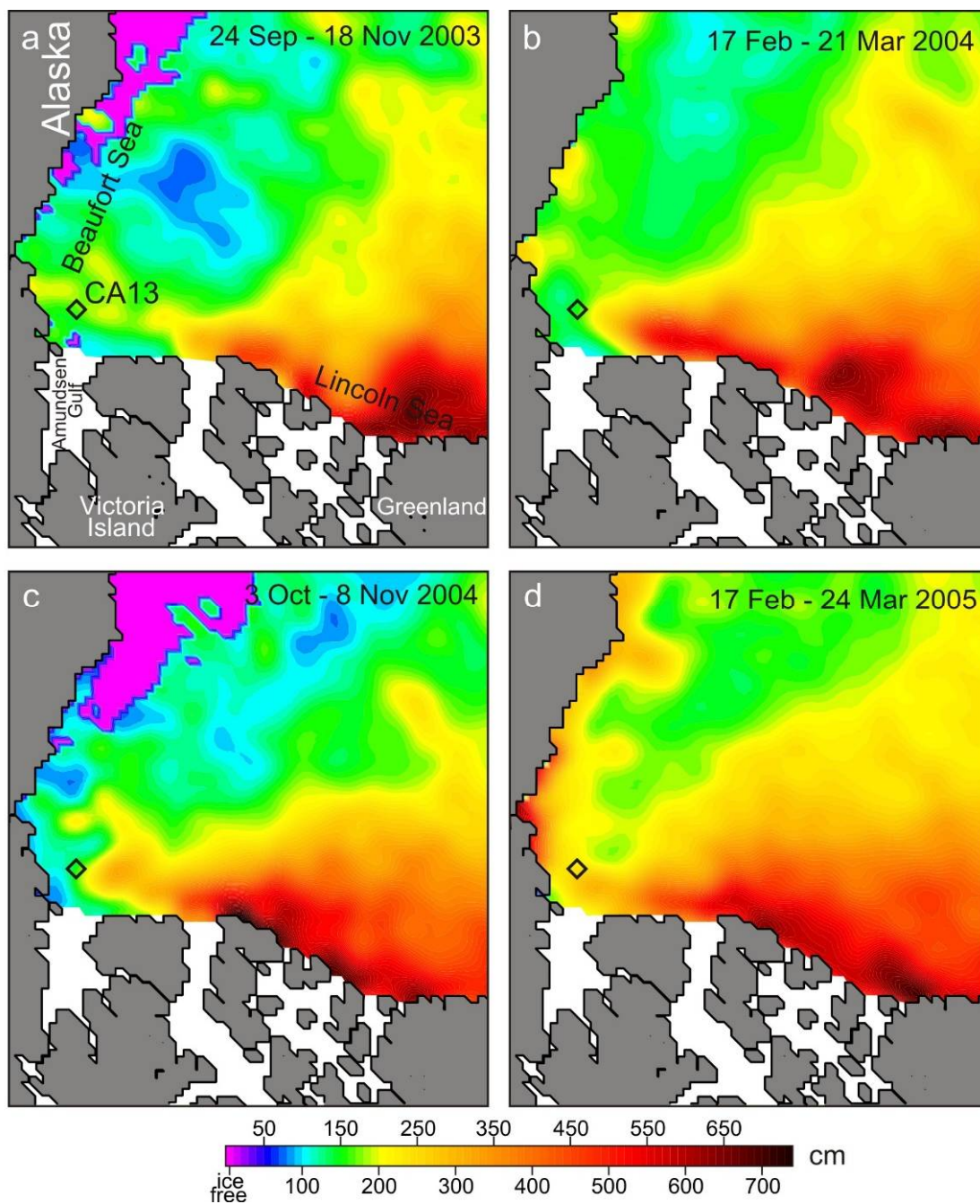


978  
979  
980  
981  
982

**Figure 4:** Spatial distribution of sea-ice thickness (m) based on model simulations using DMI's ocean and sea ice model HYCOM+CICE for February-May 2004 (top) and 2005 (bottom). The black diamonds depict mooring position.

983

984

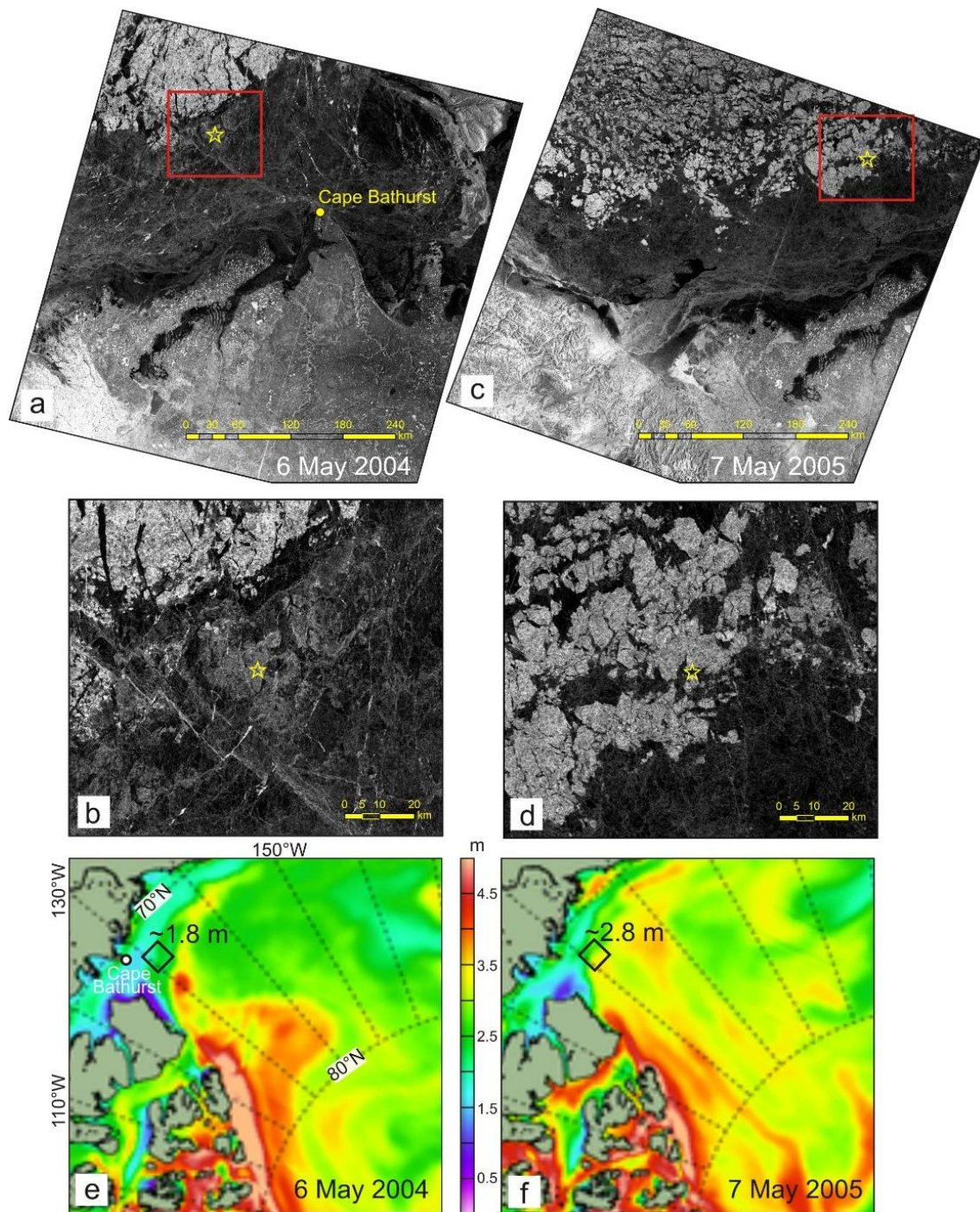


985

986 **Figure 5:** Spatial distribution of sea-ice thickness (cm) over the Canada Basin compiled using  
987 gridded sea ice thickness data from ICESat campaigns for (a) 24 September – 18 November  
988 2003, (b) 17 February – 21 March 2004, (c) 3 October – 8 November 2004 and (d) 17 February  
989 – 24 March 2005 following Kwok et al. (2009). The black diamonds depict mooring position.

990

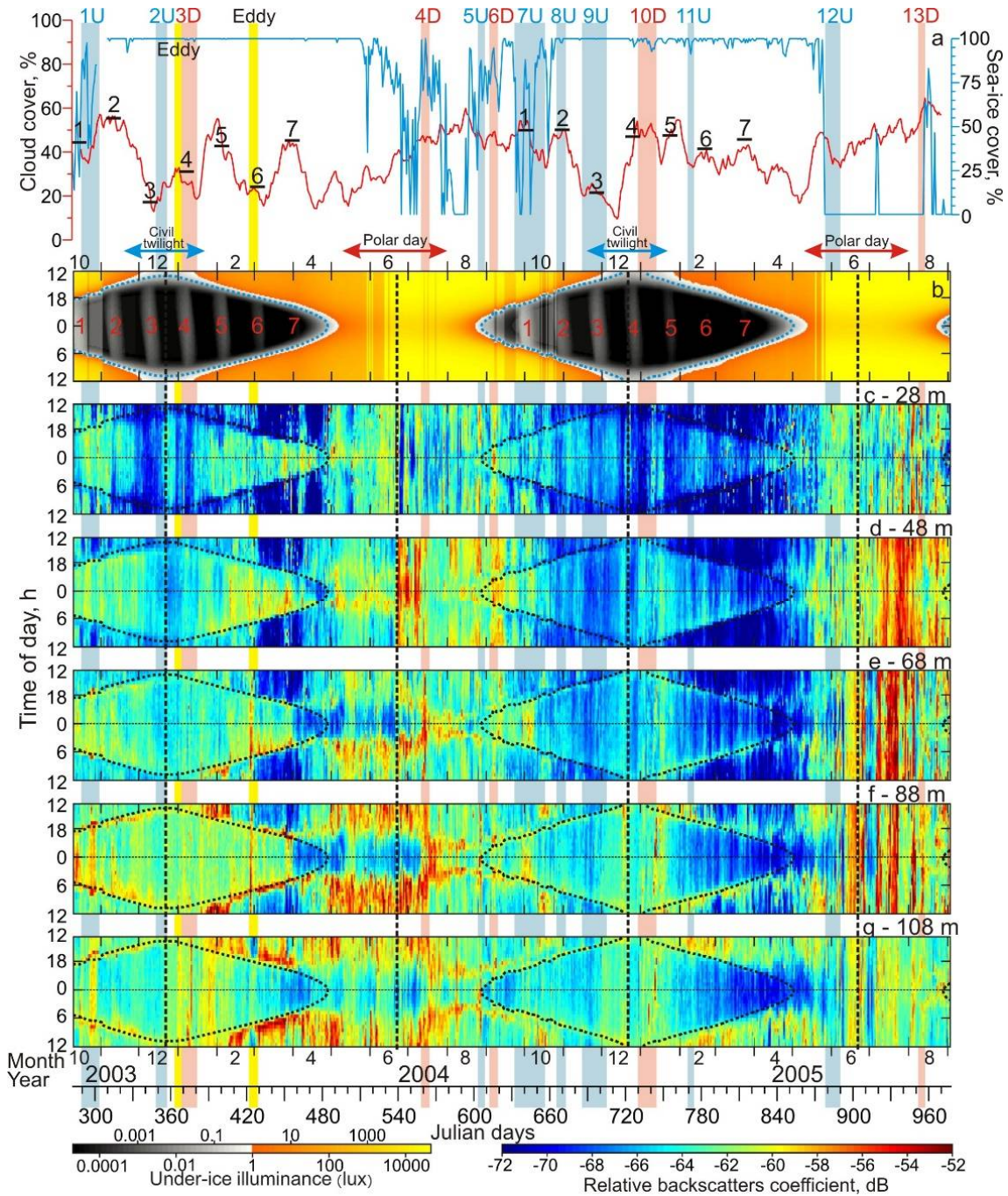




992

993 **Figure 6:** (a-d) RADARSAT satellite images taken before sea-ice breakup over the CA13  
 994 location northeast of Cape Bathurst on (a) 6 May 2004 and (c) 7 May 2005. Red rectangles  
 995 show mooring region enlarged in b and d. Yellow stars depict mooring position. The dark areas  
 996 are associated with the first-year pack ice (< 2 m thick). The lighter areas indicate the multi-  
 997 year pack ice (> 2 m thick). (e-f) Spatial distribution of sea-ice thickness (m) based on the  
 998 HYCOM+CICE model simulations for (e) 6 May 2004 and (f) 7 May 2005. The black  
 999 diamonds depict mooring position. Numbers show approximate sea-ice thickness.

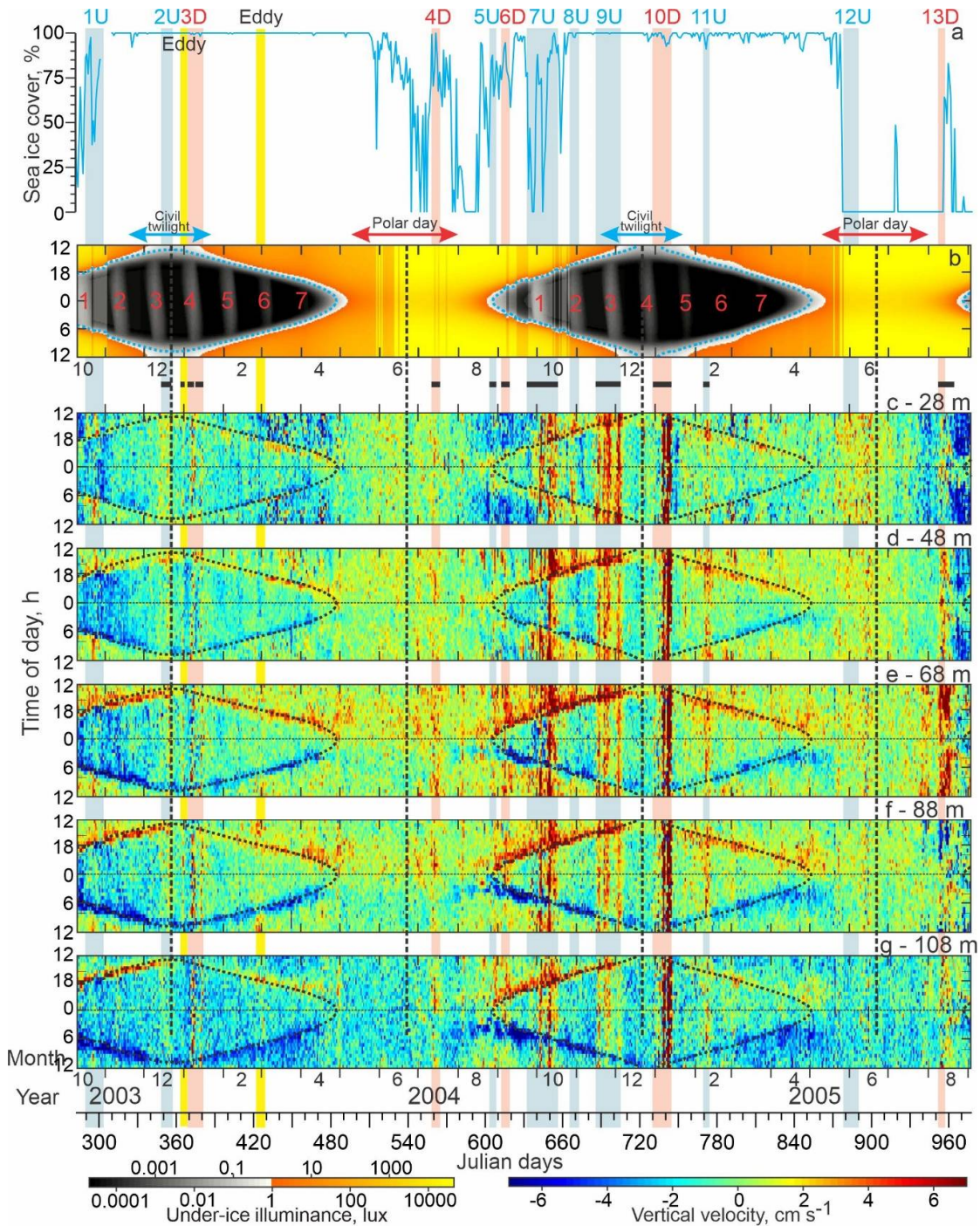




1002 **Figure 7:** (a) Time series of sea-ice concentrations (blue, %) and 15-day running mean of total  
 1003 cloud cover (red, %). Actograms of (b) modeled under-ice illuminance (lux) based on  
 1004 HYCOM+CICE sea-ice thickness, and (c-g) MVBS (dB) at five depth levels: (c) 28 m, (d) 48  
 1005 m, (e) 68 m, (f) 88 m, and (g) 108 m. The dotted blue (b) and black (c-g) lines depicts 0.1-lux  
 1006 threshold. Red and blue arrows at the top indicate the polar day and civil twilight, respectively.  
 1007 Red numbers reference the full moon occurrences, and black horizontal segments in (a)  
 1008 indicate the mean cloud cover for these periods. Black dashed vertical lines depict solstices.  
 1009 Red and blue shading highlight the downwelling (D) and upwelling (U) events, respectively,  
 1010 with their reference numbers on the top. Yellow shading highlights eddies.



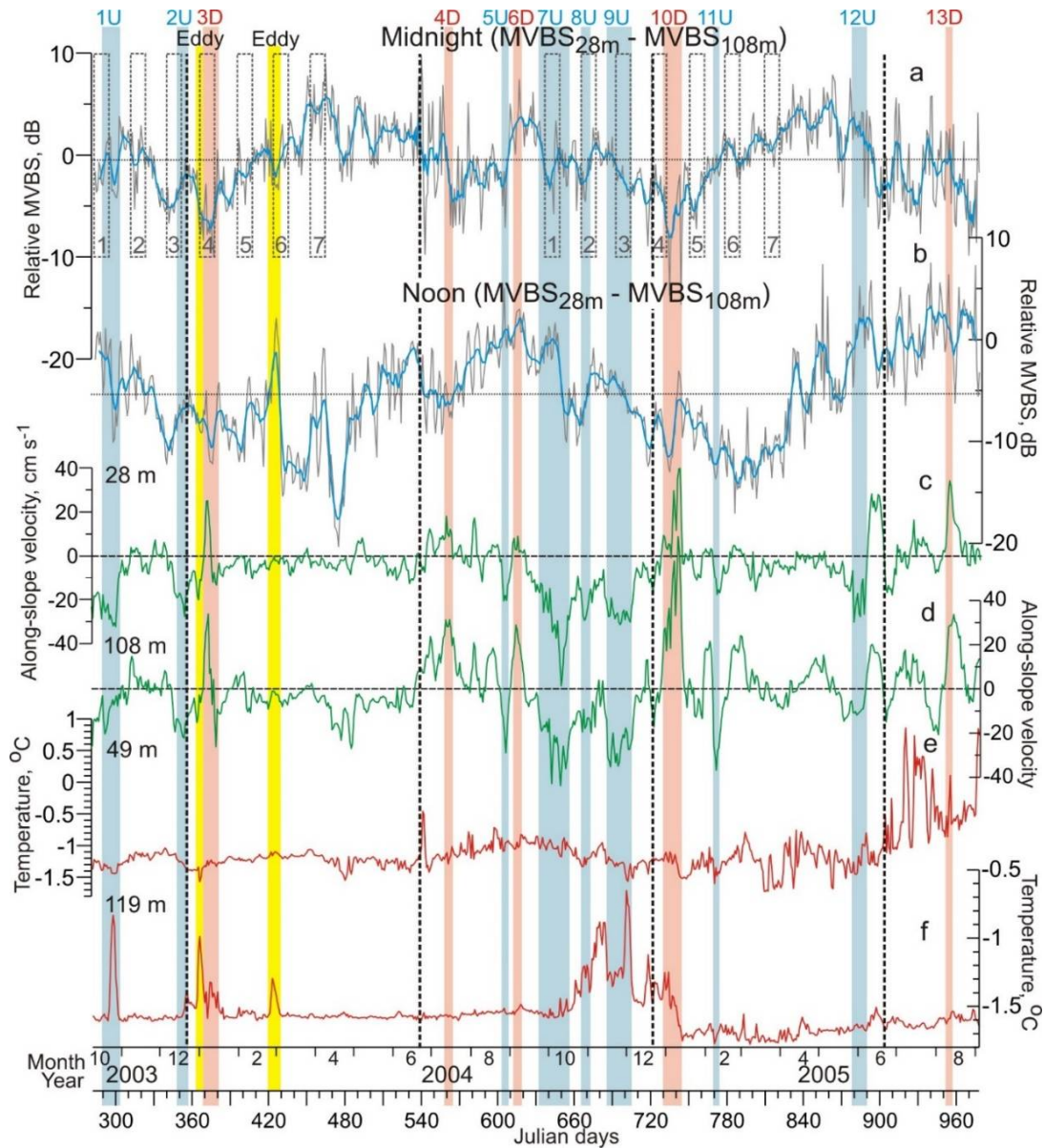
1011  
1012



1013

1014 **Figure 8:** (a) Time series of sea-ice concentrations (%). Actograms of (b) modeled under-ice  
1015 illuminance (lux) based on HYCOM+CICE sea-ice thickness, and (c-g) ADCP-measured  
1016 vertical velocity (cm s<sup>-1</sup>) at five depth levels: (c) 28 m, (d) 48 m, (e) 68 m, (f) 88 m and (g) 108  
1017 m. Positive/negative values correspond to the upward/downward flow. Horizontal black lines  
1018 at the top of panel (c) depict periods of noise in vertical velocity attributed to spatial  
1019 inhomogeneity of the flow field and errors in the ADCP tilt angle (for more details see section  
1020 3). All other designations are similar to those in Figure 7.

1021  
 1022  
 1023



1024

1025 **Figure 9:** Time series of the daily mean relative MVBS (dB) from 28 m to 108 m depth for the  
 1026 astronomic (a) midnight and (b) noon  $\pm 1$  h, along-slope (positive northeastward) velocity for  
 1027 depths of (c) 28 m and (d) 108 m ( $\text{cm s}^{-1}$ ) and water temperatures ( $^{\circ}\text{C}$ ) for (e) 49 m and (f)  
 1028 119 m depth. (a-b) Blue lines show the 7-day running mean. Horizontal dotted lines show the  
 1029 2-year means. Positive/negative values correspond to MVBS gain/loss at 28/108 m depth. (a)  
 1030 Gray dashed rectangles depict the full moon occurrence  $\pm 6$  days. All other designations are  
 1031 similar to those in Figure 7.

1032  
 1033

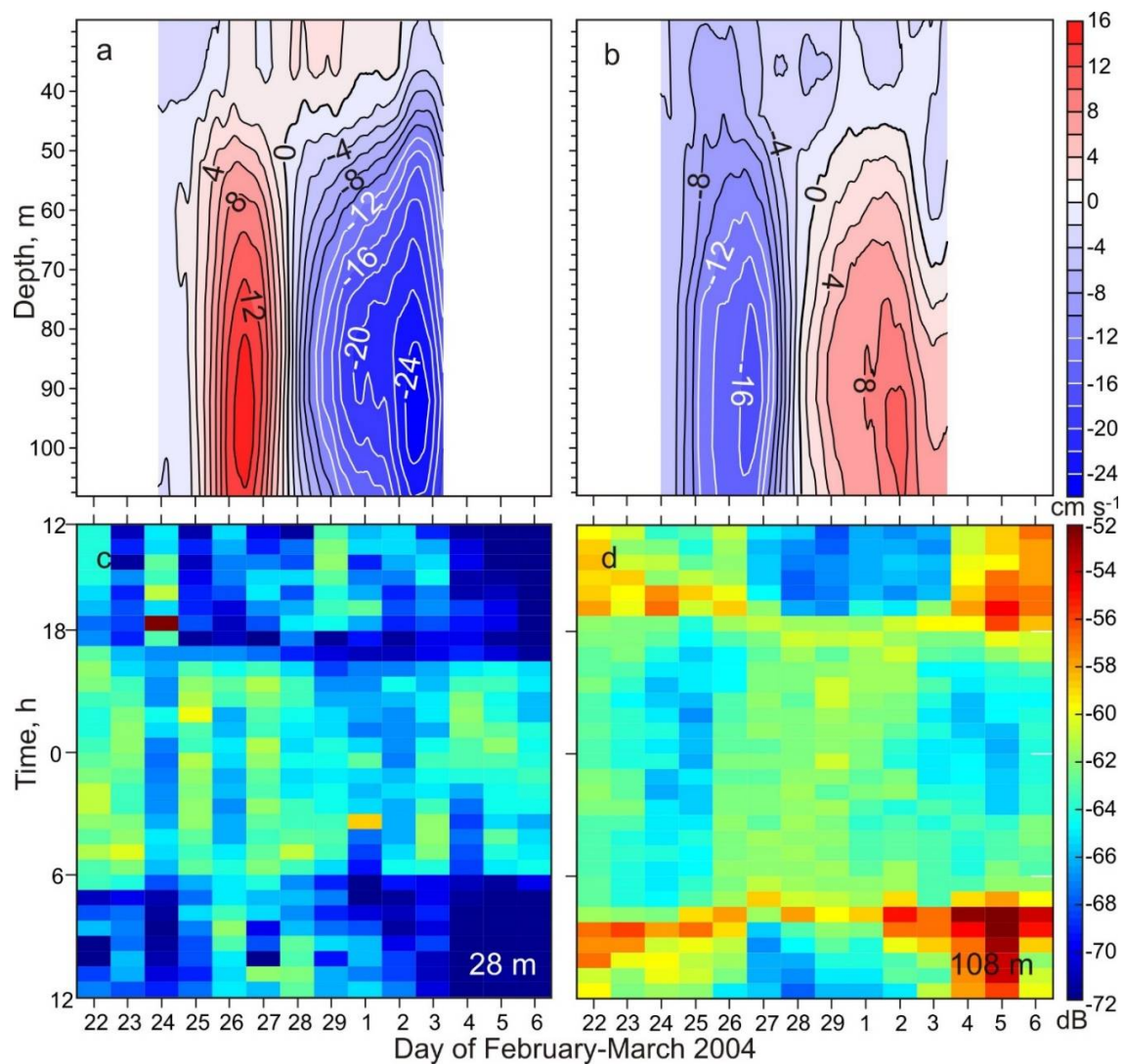


1034

1035

1036

1037



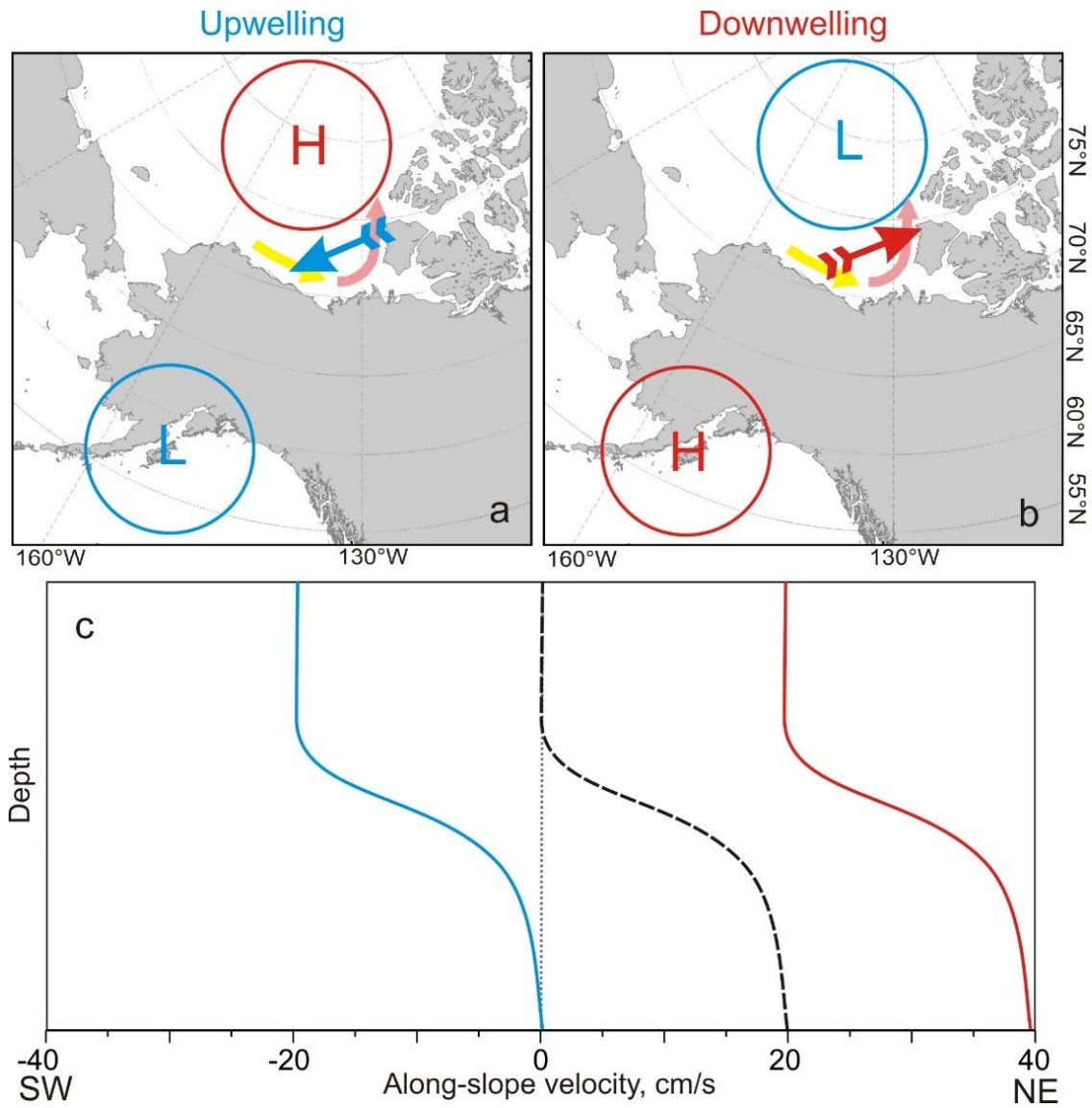
1038

1039 **Figure 10:** Enlarged view of the February-March 2004 eddy. (a) Zonal and (b) meridional  
1040 current ( $\text{cm s}^{-1}$ ) records as functions of depth adopted from Dmitrenko et al. (2018). (c-d)  
1041 actograms of MVBS (dB) for (c) 28m and (d) 108 m depth.

1042

1043

1044



1045

1046 **Figure 11:** Schematic depiction showing atmospheric forcing for (a) upwelling and (b)  
1047 downwelling along the eastern Beaufort Sea continental slope adopted from Kirillov et al.  
1048 (2016). Blue and red arrows indicate geostrophic wind associated with concurrence between  
1049 atmospheric low and high depicted by blue and red circles, respectively. Yellow and pink  
1050 arrows show circulation with shelfbreak jet over the western and eastern Beaufort Sea,  
1051 respectively, intensified by local downwelling. (c) Schematic depiction suggesting generation  
1052 of the surface-intensified (blue curve) and depth-intensified (red curve) along-slope currents as  
1053 a result of upwelling and downwelling, respectively, superimposed on the hypothetical bottom-  
1054 intensified shelfbreak current (black dashed curve) following Dmitrenko et al. (2018).